



Publication Year	2019
Acceptance in OA @INAF	2020-12-22T09:46:27Z
Title	First interferometric study of enhanced N-fractionation in N_2H^+ : the high-mass star-forming region IRAS 05358+3543
Authors	Colzi, L.; FONTANI, FRANCESCO; Caselli, P.; Leurini, Silvia; Bizzocchi, L.; et al.
DOI	10.1093/mnras/stz794
Handle	http://hdl.handle.net/20.500.12386/29081
Journal	MONTHLY NOTICES OF THE ROYAL ASTRONOMICAL SOCIETY
Number	485

First interferometric study of enhanced N-fractionation in N_2H^+ : the high-mass star-forming region IRAS 05358+3543

L. Colzi,^{1,2*} F. Fontani,² P. Caselli,³ S. Leurini,⁴ L. Bizzocchi³ and G. Quaià¹

¹Università degli studi di Firenze, Dipartimento di fisica e Astronomia, Via Sansone 1, I-50019 Sesto Fiorentino, Italy

²INAF – Osservatorio Astrofisico di Arcetri, Largo E. Fermi 5, I-50125 Florence, Italy

³Max-Planck-Institut für extraterrestrische Physik, Giessenbachstrasse 1, D-85748 Garching bei München, Germany

⁴INAF – Osservatorio Astronomico di Cagliari, Via della Scienza 5, Selargius CA I-09047, Italy

Accepted 2019 March 14. Received 2019 March 14; in original form 2019 January 25

ABSTRACT

Nitrogen (N)-fractionation is used as a tool to search for a link between the chemical history of the Solar system and star-forming regions. A large variation of $^{14}\text{N}/^{15}\text{N}$ is observed towards different astrophysical sources, and current chemical models cannot reproduce it. With the advent of high angular resolution radiotelescopes it is now possible to search for N-fractionation at core scales. We present IRAM NOEMA observations of the $J = 1-0$ transition of N_2H^+ , $^{15}\text{NNH}^+$, and N^{15}NH^+ towards the high-mass protocluster IRAS 05358+3543. We find $^{14}\text{N}/^{15}\text{N}$ ratios that span from ~ 100 up to ~ 220 and these values are lower or equal to those observed with single-dish observations towards the same source. Since N-fractionation changes across the studied region, this means that it is regulated by local environmental effects. We find also the possibility, for one of the four cores defined in the protocluster, to have a more abundant $^{15}\text{NNH}^+$ with respect to N^{15}NH^+ . This is another indication that current chemical models may be missing chemical reactions or may not take into account other mechanisms, like photodissociation or grain surface chemistry, that could be important.

Key words: astrochemistry – stars: formation – ISM: individual objects: IRAS 05358+3543 – ISM: molecules – radio lines: ISM.

1 INTRODUCTION

The origin of the Solar system is still a highly debated topic. Understanding the origin of the molecules in different Solar system bodies is important to have information on the protosolar nebula (PSN) from which our Sun was born. In particular, it is not clear if molecules in pristine Solar system materials, like comets or asteroids, were inherited from the cold and dense PSN or if they are the result of chemical processing within the solar protoplanetary disc.

One of the most used approaches involves measurement of the $^{14}\text{N}/^{15}\text{N}$ ratio from different molecules. The ratio measured for the PSN from the solar wind is 441 ± 6 (Marty et al. 2010), and this value is about two times larger than that measured in the terrestrial atmosphere (TA), derived from N_2 , ~ 272 (Marty, Zimmermann & Burnard 2009). Colzi et al. (2018b) derived a new $^{14}\text{N}/^{15}\text{N}$ ratio in the local interstellar medium (ISM) of 375 ± 60 , broadly consistent with the PSN value and consistent with the values predicted by the Galactic chemical evolution model of Romano et al. (2017). The PSN value is also larger than that measured in some comets (~ 140 , observed in CN, HCN, and NH_2 ; average value from Hily-Blant

et al. 2017 and reference therein) and in carbonaceous chondrites ($\sim 50-250$; e.g. van Kooten et al. 2017). van Kooten et al. (2017) found also a different ^{15}N -enrichment between the amine groups and the nitrile functional groups in the lithic clasts of the Isheyevo carbonaceous chondrite of their study. New measurements also confirm the trend of low $^{14}\text{N}/^{15}\text{N}$ values in pristine Solar system materials. In fact, Yang et al. (2017) derived a $^{14}\text{N}/^{15}\text{N} = 130 \pm 15$ from CN and $^{14}\text{N}/^{15}\text{N} = 140 \pm 28$ from NH_2 in the outbursting comet C/2015 ER61. Moreover, McGeoch et al. (2018) determined, with a study of polymers of amino acids, in the Allende and Acfer 086 meteorites, $^{14}\text{N}/^{15}\text{N}$ of ~ 200 and ~ 140 , respectively.

The relation between the ^{15}N -enrichments in pristine Solar system material and the natal core is still uncertain, and probably these differences are also coming from different nitrogen reservoirs. $^{14}\text{N}/^{15}\text{N}$ ratios were measured through observations towards both low- and high-mass star-forming regions from different molecules: HCN and HNC (e.g. Hily-Blant et al. 2013; Zeng et al. 2017; Colzi et al. 2018a,b; Magalhães et al. 2018), N_2H^+ (e.g. Daniel et al. 2016), and NH_3 (e.g. Gerin et al. 2009). None of these values are consistent with the antifractionation ($^{14}\text{N}/^{15}\text{N} > 500$) observed with N_2H^+ by Bizzocchi et al. (2013), Fontani et al. (2015), and Redaelli et al. (2018). Moreover, a difference between nitrile molecules (i.e. CN-bearing, such as HCN/HNC) and hydrogenated N-bearing molecules (e.g. NH_3 and N_2H^+) has been claimed, e.g. by Hily-

* E-mail: colzi@arcetri.astro.it

Blant et al. (2013) and Wampfler et al. (2014). A different behaviour between HCN/HNC and N_2H^+ is also apparent in massive star-forming regions. In fact, Fontani et al. (2015) found a larger dispersion of values from N_2H^+ (from 180 up to 1300), with respect to the values found by Colzi et al. (2018a) from HCN and HNC (from 250 up to 650) in the same sample of sources in which were also performed other astrochemical studies (e.g. Colzi et al. 2018a; Fontani et al. 2018) and Mininni et al. 2018.

A summary of the measured $^{14}\text{N}/^{15}\text{N}$ ratios from different molecules can be found in Wirström et al. (2016).

Guzmán et al. (2017) have measured the $^{14}\text{N}/^{15}\text{N}$ from HCN towards six protoplanetary discs, and found that most of them show $^{14}\text{N}/^{15}\text{N}$ consistent with comet-like values (80–160, with an average value of 111 ± 9). However, Hily-Blant et al. (2017) measured a $\text{CN}/\text{C}^{15}\text{N}$ ratio of 323 ± 30 in the disc orbiting the nearby young star TW Hya, and they proposed the CN as a possible present-day reservoir of nitrogen in the solar neighbourhood.

From a theoretical point of view, two possible mechanisms were proposed to explain ^{15}N -fractionation: isotope-exchange reactions, favoured at low temperatures ($T < 20\text{K}$; e.g. Roueff, Loison & Hickson 2015; Wirström & Charnley 2018; Loison et al. 2019), or selective photodissociation of $^{14}\text{N}/^{15}\text{N}$ over $^{14}\text{N}_2$ (Heays et al. 2014), favoured in the external layers of the discs exposed directly to the illumination of the central (proto-)star. Visser, Facchini & Heays (2018) confirmed that isotope-selective photodissociation could be crucial to understand the N-fractionation in protoplanetary discs, especially those exposed to strong irradiation fields. In particular, for N_2H^+ , this is true if the dominant fractionation mechanism is reactions with atomic N.

In this work we will focus on N_2H^+ . Terzieva & Herbst (2000) proposed that the reactions that cause most of the ^{15}N -enrichment in N_2H^+ are



However, the most recent chemical models have challenged this scenario, due to the recent discovery that reactions (1a) and (1b) do not occur in cold environments due to the presence of an entrance barrier (Roueff et al. 2015; Wirström & Charnley 2018). These chemical models fail to reproduce both the antifractionation (i.e. $^{14}\text{N}/^{15}\text{N} > 500$) measured in cold pre-stellar cores (Redaelli et al. 2018) and the large spread of values measured from different high-mass star-forming regions (Fontani et al. 2015). This also suggests that chemical reactions may still be missing in existing models, or that the ^{15}N -enrichment (or the contrary, i.e. ^{15}N -depletion, which causes antifractionation) is a local phenomenon occurring in spatial regions smaller than the beam size of single-dish observations described above. In fact, for example with the single-dish observations made by Fontani et al. (2015), the isotopic ratios obtained were average values over angular sizes of ~ 30 arcsec, which hence include both the large-scale envelope and the dense core(s) embedded within it. A more recent chemical model of Furuya & Aikawa (2018) proposed that antifractionation could be explained introducing other mechanisms in chemical models, like isotope-selective photodissociation of N_2 and grain surface chemistry. We will discuss this point in Section 4.2.

In this work we report, for the first time, an interferometric analysis of the isotopic ratio $^{14}\text{N}/^{15}\text{N}$ towards the high-mass star-forming protocluster IRAS 05358+3543 (hereafter 05358) from N_2H^+ . We discuss the possible different N-fractionation between

$^{15}\text{NNH}^+$ and N^{15}NH^+ and the possible ^{15}N -enrichment at core scales (~ 5 arcsec). N-fractionation in N_2H^+ towards this source was already studied by Fontani et al. (2015), who analysed IRAM-30m observations towards a sample of 26 high-mass star-forming regions, including 05358. In particular, for this source they found that the $^{14}\text{N}/^{15}\text{N}$ is lower (~ 200) than in the other massive star-forming regions.

The source and the observations are described in Section 2, the results are presented in Section 3, and a discussion of the results is presented in Section 4.

2 SOURCE AND OBSERVATIONS

05358 is part of a sample of 69 high-mass protostellar objects studied by Sridharan et al. (2002) and Beuther et al. (2002b,c,d) in the millimetre wavelengths. The source lies at a distance of 1.8 kpc in the Auriga molecular cloud complex (Heyer et al. 1996), in the Perseus spiral arm of the Milky Way, and has a bolometric luminosity of $6300 L_{\odot}$ (Snell, Dickman & Huang 1990). The source is part of a complex group of H II regions: SH 235 is the brightest of four optical H II regions and it is excited by the O9.5 star BD+351201 (Georgelin 1975). The source 05358 is associated with the H II region SH 233, which is approximately 25 arcmin west and 5 arcmin south of SH 235.

As evidence for massive star formation, the source is associated with maser emissions (e.g. Minier, Booth & Conway 2000; Hu et al. 2016) and massive outflows (e.g. Beuther et al. 2002a; Ginsburg et al. 2009). Beuther et al. (2007) resolved 05358 in at least three continuum sub-sources:

- mm1: It has a typical spectrum of a young massive protostar where the central source has already started hydrogen burning. The source could be a B1 zero-age main-sequence star, with a luminosity of $\sim 10^{3.72} L_{\odot}$ and a stellar mass of $\sim 13 M_{\odot}$ (Lang 1992). From the vicinity of the source, a collimated outflow is ejected with a rate of $6 \times 10^{-4} M_{\odot} \text{yr}^{-1}$ (Beuther et al. 2002a), indicating that the protostar is still accreting gas. Moreover, the source is associated with a 8.3 GHz emission (VLA data) that is likely from a hypercompact H II region. The main (sub)mm continuum source, which is at the centre of two molecular outflows (Beuther et al. 2002a), is resolved in two separate (sub)mm continuum peaks, mm1a and mm1b.

- mm2: It consists of at least two sub-sources, mm2a and mm2b, and the position of mm2b shifts from 1.2 mm to 875 μm . There is also the presence of other peaks (mm2c and mm2d). The source mm2a is detected as a compact one and this could indicate that only this source is a star-forming region, while the others could be transient sources caused by the multiple outflow system in the region.

- mm3: For this source there is neither cm nor compact line detection (Leurini et al. 2007) and then it could be a very cold massive core in an early evolutionary stage. The grey-body function used to fit the SED is constrained by the high-frequency (~ 700 GHz) measurement by Beuther et al. (2007) to dust temperatures below 20 K.

Table 1 contains the source coordinates.

We carried on observations with the IRAM NOEMA Interferometer of the $J = 1-0$ transition of N_2H^+ , $^{15}\text{NNH}^+$, and N^{15}NH^+ towards 05358. The rest frequencies are 93.1734 (Cazzoli et al. 2012), 90.2638, and 91.2057 GHz (Dore et al. 2009), for the $J = 1-0$ transition of N_2H^+ , $^{15}\text{NNH}^+$, and N^{15}NH^+ , respectively. In Table 2 the energy of the upper levels, the Einstein coefficients, and

Table 1. Coordinates of the dust continuum sources as observed by Beuther et al. (2007).

Source	RA [J2000] (h m s)	Dec. [J2000] (° ′ ″)
mm1a	05:39:13.08	35:45:51.3
mm1b	05:39:13.13	35:45:50.8
mm2	05:39:12.76	35:45:51.3
mm3	05:39:12.50	35:45:54.9
mm4 ^a	05:39:12.46	35:45:40.9

^aSource that is discovered in this work and it was not studied by Beuther et al. (2007).

Table 2. Molecular transitions of the $J = 1-0$ transition of N_2H^+ , $^{15}NNH^+$, and $N^{15}NH^+$.

Molecule	Frequency (GHz)	Transition	E_U (K)	$\log_{10}(A_{ij}^a)$
N_2H^+ ^b	93.1734	$J = 1-0$	4.5	-4.44034
$^{15}NNH^+$	90.2635	$J = 1-0, F = 1-1$	4.3	-4.48168
	90.2639	$J = 1-0, F = 2-1$		
	90.2645	$J = 1-0, F = 0-1$		
$N^{15}NH^+$	91.2043	$J = 1-0, F = 1-1$	4.4	-4.46810
	91.2060	$J = 1-0, F = 2-1$		
	91.2086	$J = 1-0, F = 0-1$		

^aEinstein coefficient of the transition.

^bFor this molecule only the rotational transition between level i and j is given, since with our spectral set-up we were not able to resolve the hyperfine structure.

the rest frequencies of each hyperfine transition are given, except for $N_2H^+(1-0)$, for which only the rotational frequency is given, since the hyperfine structure is not resolved in our spectra. To discuss our results, in Section 4.1 we will also use the averaged emission map of the $J = 5-4, K = 0,1$ transitions of CH_3CN . The rest frequencies are 91.987 and 91.985 GHz, respectively (Cazzoli & Puzzarini 2006). Because these lines were in the same spectral band as the $J = 1-0$ transition of N_2H^+ , the synthesized beam, spectral resolution, and rms are the same.

Observations were carried out in four days from 2016 September 29 to November 3, with eight antennas in C and D configurations, providing baselines between 15 and 240 m, corresponding to an angular resolution of ~ 3.1 arcsec \times 3 arcsec. The amount of precipitable water vapour was generally between 5 and 10 mm. Visibility amplitudes and phases were calibrated on 0552+398 and 0548+378. The absolute flux density scale was calibrated on MWC349 and LKHA101. The bandpass calibration was performed on 3C 84 or 3C 454.3. To incorporate short spacings to the interferometric maps, we have reduced and analysed IRAM-30m observations of the $J = 1-0$ transition of N_2H^+ , $^{15}NNH^+$, and $N^{15}NH^+$. These observations were carried out on 2017 March 5, 6, and 7. We have obtained large-scale maps on an angular region of ~ 120 arcsec, that is about twice the NOEMA primary beam at the frequency of the $N_2H^+(1-0)$ transition. The data were obtained with the on-the-fly mapping mode. The pointing was checked every hour on nearby quasars. The focus was checked at the start of the observations and after sunset. Creation of the synthetic visibilities and merging of the two data sets were performed through standard procedures available in the GILDAS software package MAPPING.

Table 3. Observational parameters.

Spw	Synthesized beam (arcsec \times arcsec)	PA (°)	Δv (km s ⁻¹)	rms (mJy beam ⁻¹)
Continuum	3.01×2.61	-110.18	-	0.2
N_2H^+	3.04×2.64	-109.5	6.45	0.5
$^{15}NNH^+$	3.12×3.08	-41.91	0.5	7
$N^{15}NH^+$	3.12×3.08	-41.91	0.5	7

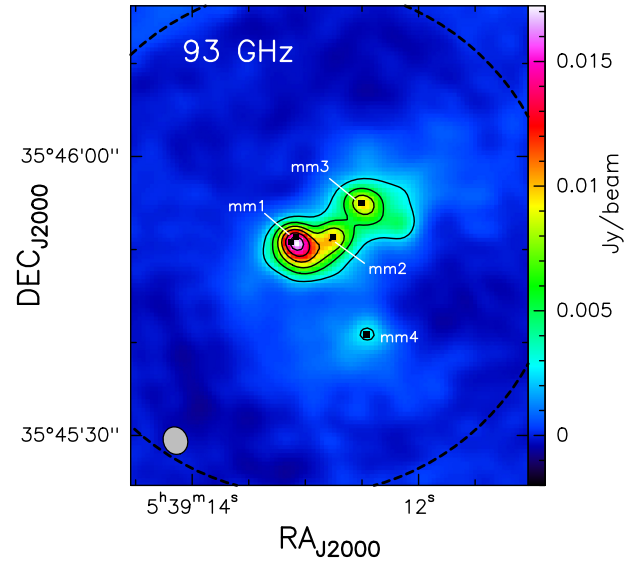


Figure 1. 93 GHz continuum emission obtained with IRAM NOEMA. The first contour level is the 15 per cent of the maximum value of the map, which corresponds to ~ 17 mJy beam⁻¹. The other contour levels are the 30 per cent, 45 per cent, 60 per cent, 75 per cent, and 90 per cent of the maximum value, respectively. The black squares indicate the position of mm1a, mm1b, mm2, mm3, and mm4 as given in the text and in Table 1. The dashed circle represents the NOEMA field of view and the synthesized beam is the ellipse indicated in the lower left corner.

Calibration and imaging were performed using the CLIC and MAPPING software of the GILDAS package.¹ The synthesized beam, the final velocity resolution, and the rms (root mean square) of the data cubes are given in Table 3. The analysis of the data was done with the MADCUBA² software package. For the analysis we have used the spectroscopic parameters from the CDMS molecular catalogue³ (Müller et al. 2001, 2005; Endres et al. 2016).

3 RESULTS

3.1 Continuum map

In Fig. 1 the 3 mm continuum map towards the source is shown. With this map we are able to distinguish the already known continuum millimetre sources mm1, mm2, and mm3 (Beuther et al. 2007). However, we are not able to resolve mm1 as a binary system composed of mm1a and mm1b (Table 1) because

¹The GILDAS software is available at <http://www.iram.fr/IRAMFR/GILDAS>

²Madrid Data Cube Analysis on ImageJ is a software developed in the Center of Astrobiology (Madrid, INTA-CSIC) to visualize and analyse single spectra and data cubes (Martín et al., in prep.; Rivilla et al. 2016; Rivilla et al. 2017).

³<http://cdms.astro.uni-koeln.de/classic/>

of the insufficient spatial resolution (Table 3). Moreover, we have observed the continuum emission of a new millimetre source (mm4) at right ascension $\alpha_{2000} = 05^{\text{h}}:39^{\text{m}}:12.46$ and declination $\delta_{2000} = 35^{\circ}:45':40''.9$. Since this source is out of the primary beam at 1 mm, it was not analysed by Beuther et al. (2007), who focused their work on characterising the properties of 05358 at the centre of the field of view.

3.2 Morphology of N_2H^+ and ^{15}N isotopologue emission

In Fig. 2 we show the averaged emission map of $\text{N}_2\text{H}^+(1-0)$, which arises mainly from three cores: one associated with both mm1 and mm2 not resolved, another associated with mm3, and finally one associated with mm4. We have also highlighted the presence of two other $\text{N}_2\text{H}^+(1-0)$ emission regions (A and B) and we will discuss them in Section 4.1. It can also be noted that the $\text{N}_2\text{H}^+(1-0)$ emission peaks are shifted by $\sim 2-3$ arcsec with respect to the mm1, mm2, and mm3 continuum sources. We will discuss this result in Section 4.1.

In Fig. 3 the averaged emission maps of the $^{15}\text{NNH}^+(1-0)$ and $\text{N}^{15}\text{NH}^+(1-0)$ transitions are shown. They are obtained by integrating the lines over the channels with signal, above the 3σ level, in the Narrow spectra. In particular, for $\text{N}^{15}\text{NH}^+(1-0)$ we were able to resolve the hyperfine structure in three distinct components (see Table 2). However, since the $J = 1-0$, $F = 1-1$, and $J = 1-0$, $F = 0-1$ transitions are near the noise level, we have decided to create the emission map integrating only over the channels that correspond to the strongest component, namely the $J = 1-0$, $F = 2-1$ transition. Moreover, in Fig. 3 the blue contours correspond to the polygons from which we have extracted the spectra, in order to derive the total column densities of the three molecules, and the corresponding $^{14}\text{N}/^{15}\text{N}$ ratios, in eight different regions in 05358. The polygons are defined from the 5σ of the corresponding averaged map. In particular, P1a, P2a, P3a, and P4a correspond to a value of $5 \times 0.72 \text{ mJy beam}^{-1}$ (from $^{15}\text{NNH}^+$; left-hand panel

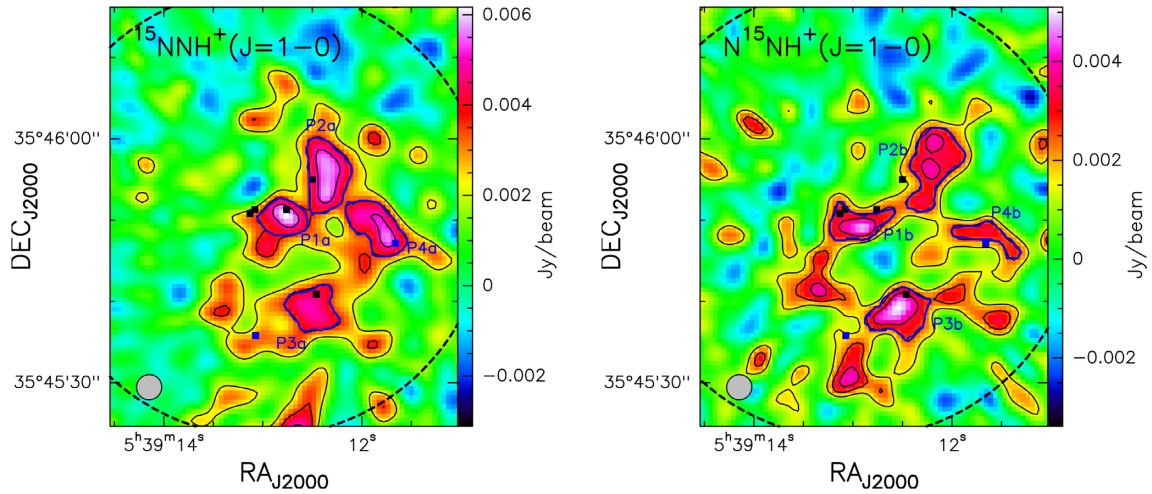


Figure 3. *Left-hand panel:* averaged map of $^{15}\text{NNH}^+(1-0)$ at 90.26 GHz (velocity range between -19.3 and -14.2 km s^{-1}) obtained from the Narrow correlator. The black contour levels are 3, 5, and 7 times the 1σ rms of the map, equal to $\sim 5 \times 0.72 \text{ mJy beam}^{-1}$. *Right-hand panel:* averaged map of the $J = 1-0$, $F = 2-1$ transition of N^{15}NH^+ (main hyperfine component) at 91.20 GHz (velocity range between -19.5 and -15 km s^{-1}) obtained from the Narrow correlator. The black contour levels are 3, 5, and 7 times the 1σ rms of the map, equal to $\sim 5 \times 0.5 \text{ mJy beam}^{-1}$. In both panels, the blue contours correspond to the 5σ level of the averaged maps, from which the spectra have been extracted: P1a, P2a, P3a, and P4a from $^{15}\text{NNH}^+$ and P1b, P2b, P3b, and P4b from N^{15}NH^+ . The black and blue squares indicate the positions of the continuum sources and the N_2H^+ peak positions (A and B), respectively, as in Fig. 2. The dashed circle represents the NOEMA field of view and the synthesized beam is the ellipse indicated in the lower left corner.

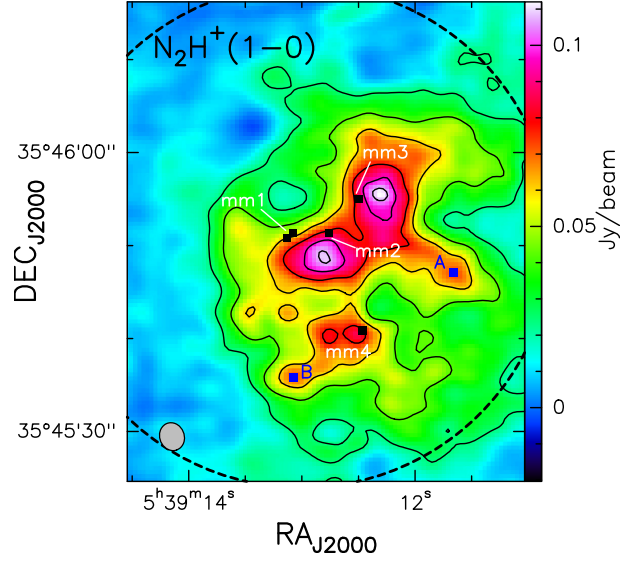


Figure 2. Averaged map of $\text{N}_2\text{H}^+(1-0)$ at 93.1734 GHz (velocity range between -34.6 and -0.1 km s^{-1}) obtained from the Widex correlator. The contour levels are 4, 7, 10, 13, 16, and 18 times the 1σ rms of the map, equal to $\sim 6 \text{ mJy beam}^{-1}$. The black squares indicate the position of mm1a, mm1b, mm2, mm3, and mm4 as given in the text and in Table 1. The blue squares correspond to the $\text{N}_2\text{H}^+(1-0)$ emission peaks, A and B, described in the text. The dashed circle represents the NOEMA field of view and the synthesized beam is the ellipse indicated in the lower left corner.

of Fig. 3), while P1b, P2b, P3b, and P4b correspond to a value of $5 \times 0.5 \text{ mJy beam}^{-1}$ (from N^{15}NH^+ ; right-hand panel of Fig. 3).

We have also extracted spectra from polygons defined as the intersection of the 5σ of the two ^{15}N -isotopologue-averaged maps (I1, I2, I3, and I4; left panel of Fig. 4). This has been done in order to compare the $^{14}\text{N}/^{15}\text{N}$ ratios obtained from $^{15}\text{NNH}^+$ and N^{15}NH^+ from the same regions of the source. Finally, we have decided to estimate the $^{14}\text{N}/^{15}\text{N}$ ratios in the regions defined in the right-hand

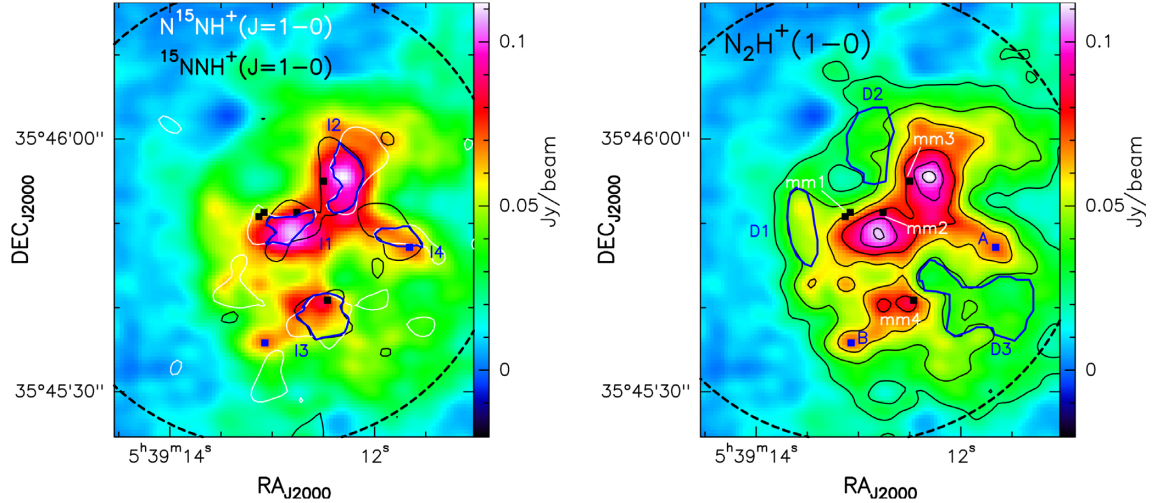


Figure 4. *Left-hand panel:* The colours are the averaged emission of $N_2H^+(1-0)$. The black contours are the 5σ levels of $^{15}NNH^+(1-0)$ averaged emission and the white contours are the 5σ levels of $N^{15}NH^+(1-0)$ averaged emission: in blue the intersection of the black and white contours (I1, I2, I3, and I4). *Right-hand panel:* the same as Fig. 2. The blue contours define three different zones D1, D2, and D3, in the diffuse N_2H^+ envelope surrounding the dense condensations identified in the left-hand panel and in Fig. 3. In both panels, the black and blue squares indicate the positions of the continuum sources and the N_2H^+ peak positions (A and B), respectively, as in Fig. 2. The dashed circle represents the NOEMA field of view.

panel of Fig. 4, D1, D2 and D3, less bright and corresponding to diffuse N_2H^+ emission.

3.3 Fitting procedure and column density calculation

To fit the lines and to compute the total column densities from the extracted spectra we have used MADCUBA assuming local thermal equilibrium (LTE) conditions. This is a reasonable assumption since the observed cores present volume densities of the order of 10^6 cm^{-3} (see Beuther et al. 2007), that is higher than the critical densities of the observed lines ($\sim 1.5\text{--}2 \times 10^5 \text{ cm}^{-3}$, assuming kinetic temperatures from 20 K up to 50 K).

The MADCUBA-AUTOFIT tool takes into account four parameters to create a synthetic LTE line profile: total column density (N), excitation temperature (T_{ex}), peak velocity (v), and full width at half-maximum (FWHM). We have fitted all the lines fixing the T_{ex} . We have performed the analysis with different T_{ex} values (20, 30, 40, and 50 K) since we had only one transition for each molecule and we were not able to derive it directly from the data. These temperature values are also consistent with the kinetic temperatures derived for 05358 from $NH_3(1,1)$ by Lu et al. (2014). Leaving free the other parameters (N , v , and FWHM) the AUTOFIT tool compares the LTE synthetic spectra with the observed spectra and provides the best non-linear least-squared fit using the Levenberg–Marquardt algorithm. When the algorithm converges, it also provides the associated errors to the parameters. From these parameters, the tool also calculates the line opacity between levels i and j , τ_{ij} (see equations 1 and 2 in Rivilla et al. 2019).

The three lines that we have observed, the $N_2H^+(1-0)$, $^{15}NNH^+(1-0)$, and $N^{15}NH^+(1-0)$ transitions, have hyperfine structure. We can resolve it only for $N^{15}NH^+(1-0)$ since the line width found ($\sim 2 \text{ km s}^{-1}$) is smaller than the separation in velocity of the hyperfine components (e.g. Fig. 5). However, we have fitted the spectra of both the $^{15}NNH^+(1-0)$ and $N^{15}NH^+(1-0)$ transitions taking the hyperfine structure into account, in order to be consistent with the analysis of the two different ^{15}N isotopologues of N_2H^+ . Conversely, for $N_2H^+(1-0)$ we have performed the analysis taking into account only the rotational transition $J = 1-0$, as if it was

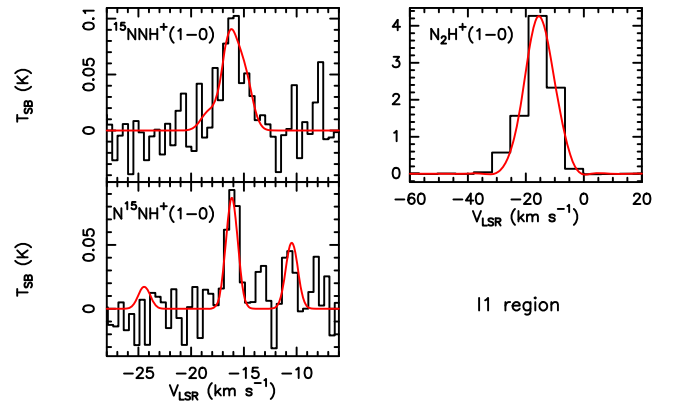


Figure 5. Example of spectra extracted from the region I1 (see left-hand panel of Fig. 4) in all the detected transitions: $^{15}NNH^+(1-0)$ (top left), $N^{15}NH^+(1-0)$ (bottom left), and $N_2H^+(1-0)$ (top right). For each spectrum the x-axis represents the systemic velocity of the source. The y-axis shows the intensity in synthesized beam temperature units. The red curves are the best fits obtained with MADCUBA (from the method described in Section 3.3). Spectra extracted from the other intersecting regions (I2–I4) are shown in Appendix A2.

a single line. We did this because the low spectral resolution ($\sim 6.5 \text{ km s}^{-1}$) permits the convergence of the fits only fixing an $\text{FWHM} > 6.5 \text{ km s}^{-1}$, that is not the real one of the source ($\sim 2 \text{ km s}^{-1}$ from the fits of ^{15}N isotopologues). The fit to a single transition permits us to leave the FWHM as a free parameter and, even if the final FWHM is not reliable, the convergence of the fit is more precise. In Appendix B2 a detailed analysis demonstrates that the use of this method gives similar results of the analysis of the same N_2H^+ simulated spectrum where the hyperfine structure could be resolved, within the errors.

All the extracted spectra from the P1a–P4a, P1b–P4b, I1, I2, I3, and I4 regions, and the more diffuse N_2H^+ emission regions D1, D2, and D3 (see Section 3.2), are shown in Appendix A (A1, A2, A3 and A4). Column densities, FWHM, velocities, and opacities

derived from the fit of the extracted spectra are given in Appendix C (Tables C1, C2, C3, C4).

For the main isotopologue, N_2H^+ , we have found column densities of the order of 10^{14} cm^{-2} in all regions. In particular, column densities towards P1a and P2a are higher than those towards P3a and P4a, of a factor ~ 1.5 . The same trend is followed by P1b and P2b with respect to P3b and P4b, with a decrease of a factor ~ 3 . However, for the ^{15}N isotopologues column densities are the same in each region, within the errors, and are of the order of 10^{11} cm^{-2} – 10^{12} cm^{-2} , depending on the assumed T_{ex} . In fact, as a general trend for all the analysed molecules, N_2H^+ , $^{15}\text{NNH}^+$, and N^{15}NH^+ , the column densities increase with the T_{ex} , but their ratios remain the same, within the uncertainties.

3.3.1 Diffuse regions

The $^{15}\text{NNH}^+(1-0)$ and $\text{N}^{15}\text{NH}^+(1-0)$ transitions are not detected in any of the diffuse N_2H^+ emission regions D1, D2, and D3, except for $^{15}\text{NNH}^+(1-0)$ in D2, for which we have obtained a tentative detection (see Fig. A3). We have considered tentative detections the lines where the peak synthesized beam temperature ($T_{\text{SB}}^{\text{peak}}$) was between 2.5σ and 3σ ($2.5\sigma \leq T_{\text{SB}}^{\text{peak}} < 3\sigma$), where σ is the rms noise of the spectrum. For the non-detections, we have computed upper limits for the column densities with MADCUBA. They have been derived from the formula $3\sigma \times \Delta v / \sqrt{N_{\text{chan}}}$, where N_{chan} is the number of channels covered by the line width Δv . In particular, we have considered as Δv an average value of the FWHM derived from the same transitions towards P1a–P4a and P1b–P4b (Table C1): $\Delta v_{^{15}\text{NNH}^+} = 2.3 \pm 0.2 \text{ km s}^{-1}$ and $\Delta v_{\text{N}^{15}\text{NH}^+} = 1.7 \pm 0.4 \text{ km s}^{-1}$. The upper limits and tentative detection fit results from diffuse N_2H^+ emission regions are reported in Table C3.

3.3.2 Extracted spectra from IRAM-30m beam

In order to compare our results with those obtained by Fontani et al. (2015) with IRAM-30m observations, we have also extracted spectra from regions that correspond to the IRAM-30m beam around the sources mm1 and mm3, as defined in Table 1 (considering mm1a and mm1b at the same coordinates). This was also done in order to show how much the $^{14}\text{N}/^{15}\text{N}$ ratios change going to smaller scales with respect to those observed with single-dish observations. The IRAM-30m beam at 93 GHz is ~ 27.6 arcsec. In order to be consistent with Fontani et al. (2015), we have fitted our spectra fixing the T_{ex} equal to those used in their work: 43 K for mm1 and 18 K for mm3. We noted that even though the two main beams are partially overlapping, the dominant emission of each of the two is from the corresponding central source. The extracted spectra from regions equivalent to the IRAM-30m beam are shown in Fig. A4 and the results from the fit are listed in Table C4.

3.4 $^{14}\text{N}/^{15}\text{N}$ ratios

We have computed the $^{14}\text{N}/^{15}\text{N}$ ratios for N_2H^+ , along with the uncertainties derived propagating the error on the total column densities. In Tables 4, 5, and 6 the $^{14}\text{N}/^{15}\text{N}$ ratios for the different regions defined in Section 3.2 are given. Since the ratios are obtained from column density values obtained from observations at a different spectral resolution, we have carefully evaluated the effects of this data inhomogeneity in Appendix B. There we show

Table 4. $^{14}\text{N}/^{15}\text{N}$ ratios derived from $^{15}\text{NNH}^+$ towards P1a, P2a, P3a, and P4a (left-hand panel) and from N^{15}NH^+ towards P1b, P2b, P3b, and P4b (right-hand panel).

Source	T_{ex} (K)	$\frac{\text{N}_2\text{H}^+}{^{15}\text{NNH}^+}$	Source	T_{ex} (K)	$\frac{\text{N}_2\text{H}^+}{\text{N}^{15}\text{NH}^+}$
P1a	20	200 ± 34	P1b	20	200 ± 25
	30	186 ± 31		30	217 ± 29
	40	178 ± 29		40	212 ± 27
	50	173 ± 27		50	222 ± 30
P2a	20	180 ± 18	P2b	20	129 ± 17
	30	171 ± 17		30	120 ± 15
	40	156 ± 16		40	108 ± 13
	50	154 ± 15		50	113 ± 14
P3a	20	120 ± 18	P3b	20	100 ± 15
	30	114 ± 17		30	100 ± 16
	40	111 ± 16		40	109 ± 17
	50	109 ± 15		50	100 ± 15
P4a	20	117 ± 14	P4b	20	187 ± 33
	30	112 ± 14		30	182 ± 31
	40	120 ± 15		40	185 ± 33
	50	108 ± 12		50	185 ± 32

Table 5. $^{14}\text{N}/^{15}\text{N}$ ratios derived from $^{15}\text{NNH}^+$ and N^{15}NH^+ towards I1, I2, I3, and I4.

Source	T_{ex} (K)	$\frac{\text{N}_2\text{H}^+}{^{15}\text{NNH}^+}$	$\frac{\text{N}_2\text{H}^+}{\text{N}^{15}\text{NH}^+}$
I1	20	220 ± 32	275 ± 50
	30	214 ± 30	250 ± 41
	40	200 ± 27	257 ± 46
	50	200 ± 28	244 ± 40
I2	20	167 ± 17	143 ± 18
	30	150 ± 15	120 ± 15
	40	136 ± 13	125 ± 16
	50	146 ± 14	127 ± 16
I3	20	100 ± 13	86 ± 12
	30	114 ± 16	89 ± 13
	40	111 ± 15	91 ± 14
	50	109 ± 15	86 ± 12
I4	20	100 ± 14	140 ± 24
	30	100 ± 14	150 ± 29
	40	100 ± 15	137 ± 25
	50	93 ± 14	130 ± 23

that the different spectral resolution does not significantly affect the column densities, and hence the $^{14}\text{N}/^{15}\text{N}$ ratios.

In general, we have found values that span from ~ 100 up to ~ 220 , where the higher values are comparable with those observed with the IRAM-30m (Fontani et al. 2015). Moreover, the assumption of different T_{ex} does not change the results, which are consistent within the errors. Therefore, in the next session we will discuss the final results considering a single excitation temperature. Moreover, a different T_{ex} can change the column densities of each molecule, but does not influence their ratios, since the dependence on T_{ex} in the ratio is irrelevant when the two column densities are both computed from the (1–0) transition and the lines are not optically thick. This is supported by the fact that the ratios given in Table 4 are the same within the uncertainties, towards each region.

Table 6. $^{14}\text{N}/^{15}\text{N}$ ratios derived from $^{15}\text{NNH}^+$ and N^{15}NH^+ for D1, D2, and D3 (upper panel). In the lower panel the $^{14}\text{N}/^{15}\text{N}$ ratios derived from both $^{15}\text{NNH}^+$ and N^{15}NH^+ towards mm1 and mm3 in regions equivalent to the IRAM-30m beam are shown.

Source	T_{ex} (K)	$\frac{\text{N}_2\text{H}^+}{^{15}\text{NNH}^+}$	$\frac{\text{N}_2\text{H}^+}{\text{N}^{15}\text{NH}^+}$
D1	20	≥ 245	≥ 204
	30	≥ 231	≥ 188
	40	≥ 242	≥ 200
	50	≥ 250	≥ 204
D2	20	336 ± 96	≥ 154
	30	327 ± 91	≥ 148
	40	316 ± 87	≥ 143
	50	292 ± 77	≥ 140
D3	20	≥ 243	≥ 340
	30	≥ 250	≥ 321
	40	≥ 261	≥ 353
	50	≥ 250	≥ 333

Source	T_{ex} (K)	$\frac{\text{N}_2\text{H}^+}{^{15}\text{NNH}^+}$	$\frac{\text{N}_2\text{H}^+}{\text{N}^{15}\text{NH}^+}$
mm1	43	219 ± 22	180 ± 33
mm3	18	217 ± 23	192 ± 32

4 DISCUSSION

4.1 Comparison between line and continuum emission maps

The averaged emission maps of the $J = 1-0$ transition of N_2H^+ , $^{15}\text{NNH}^+$, and N^{15}NH^+ (Figs 2 and 3) present a shift of $\sim 2-3$ arcsec to the south-west with respect to the continuum sources. In particular this effect is stronger for mm1, mm2, and mm3 than for mm4. The overall structure of the integrated $\text{N}_2\text{H}^+(1-0)$ (and its ^{15}N isotopologues) consists of three main cores. Two of these are located to the south of the mm1 and mm2 continuum sources, and to the west of the mm3 continuum sources, while the third is located exactly to the mm4 source. Numerous studies have shown that during the collapse of a low-mass core, the CO desorbs from the grain mantles, because of the rising of the temperature, and this causes a substantial destruction of N_2H^+ (e.g. Di Francesco, André & Myers 2004). The chemical processes at work in high-mass star-forming regions are likely different from those in low-mass star-forming ones, but the destruction of N_2H^+ by CO should occur in both cases. Towards mm1 the presence of a young massive protostar is well known (see Section 2) and the displacement between the dust and the N_2H^+ peak suggests that the heating of the protostar, and probably of the molecular outflows associated with it (Beuther et al. 2002a), may have caused the desorption of CO from grain mantles and the subsequent destruction of N_2H^+ . Probably something similar is happening also around mm3, although we do not have clear evidence that star formation has already started. Moreover, the correspondence of the dust and the N_2H^+ peak towards mm4 is evidence that it is chemically less evolved and hence maybe starless. Something similar for high-mass star-forming regions has been reported towards IRAS 23033+5951 (Reid & Matthews 2008) and towards the massive protocluster AFGL 5142 (Busquet et al. 2011). To investigate this situation better, we have searched in our spectral setup for other molecules that could better trace the continuum sources and the associated star formation activity. In particular, in Fig. 6 the averaged emission map of CH_3CN ($J = 5-4, K = 0, 1$) is shown. In the left-hand panel the clear correspondence between the

3mm-continuum sources and CH_3CN can be noted; moreover, in the right-hand panel it is evident that CH_3CN and N_2H^+ do not coincide towards mm1, mm2, and mm3, while the core structure defined by the two different molecules corresponds towards mm4. Moreover, the asymmetry of N_2H^+ around the millimetre continuum sources could be due to the presence of the interaction with the gas of the complex group of H II regions located in the north-east. However, we do not have observational proof of this point and it needs to be tested.

As already mentioned in Section 3.2, in the western and the south-eastern part of the cluster, two other N_2H^+ emission zones are present. In particular, A corresponds to a core structure in the ^{15}N isotopologue maps (P4a and P4b in Fig. 3) and also to one of the emission peaks of the high-density tracer H^{13}CO^+ defined in Fig. 8 of Beuther et al. (2002a), which is a high-density tracer. However, B presents a more complicated structure, probably related with the presence of multiple outflows in the whole region (outflow A in Beuther et al. 2002a). Leurini et al. (2011) discussed the $\text{N}_2\text{H}^+(1-0)$ emission towards the IRDC G351.77–0.51 and they found a velocity gradient on large scale, probably associated with outflows detected in CO. Although N_2H^+ is seldom associated with outflows, this could be due to an interaction of outflow shocks with the molecular envelope (traced also by N_2H^+). A similar situation was detected in the same transitions towards the class 0 object IRAM 04191+1522 by Lee, Ho & White (2005). Moreover, Codella et al. (2013) present the first detection of N_2H^+ towards a low-mass protostellar outflow, L1157-B1, a bow-shock, at ~ 0.1 pc from the protostellar cocoon L1157.

4.2 Is N-fractionation a core-scale effect?

Fontani et al. (2015) have derived, with the IRAM-30m radiotelescope, $^{14}\text{N}/^{15}\text{N}$ ratios of 190 ± 20 with $^{15}\text{NNH}^+$ and of 180 ± 23 with N^{15}NH^+ towards mm1, and of 210 ± 12 with $^{15}\text{NNH}^+$ and of 180 ± 13 with N^{15}NH^+ towards mm3. Extracting the spectra in regions equivalent to the IRAM-30m beam at 93 GHz, we have derived the $^{14}\text{N}/^{15}\text{N}$ ratios listed in the lower panel of Table 6. These are consistent with the results obtained with the single-dish telescope, within the errors. A comparison of these results with the $^{14}\text{N}/^{15}\text{N}$ ratios obtained towards P1a, P2a, P3a, and P4a and towards P1b, P2b, P3b, and P4b is shown in Fig. 7. In particular, it is evident from the left-hand panel of Fig. 7 that there is a ^{15}N enrichment (i.e. a $^{14}\text{N}/^{15}\text{N}$ ratio significantly lower) towards P2a, P3a, and P4a. The same happens towards P2b and P3b (right-hand panel of Fig. 7). This means that at higher angular resolution, where the core scales can be resolved, it is possible to reveal a different N-fractionation with respect to that observed with a single-dish telescope and more representative of the average $^{14}\text{N}/^{15}\text{N}$ between the cores and the envelope of the whole star-forming region. This suggests that the mechanisms that produce more ^{15}N with respect to ^{14}N in N_2H^+ can occur in smaller regions and could be a local effect. The fact that towards P1a and P1b, $^{14}\text{N}/^{15}\text{N}$ values consistent with IRAM-30m observations (~ 200) are found could be explained by the fact that these regions are near an evolved high-mass source (mm1) and the chemistry could be different towards hotter gas. Moreover, the different $^{14}\text{N}/^{15}\text{N}$ ratios between P4a and P4b, ~ 115 and ~ 185 , respectively, could be due to a different behaviour of the two ^{15}N isotopologues, but we will discuss about this in the next section.

In general, the lower $^{14}\text{N}/^{15}\text{N}$ ratios of $\sim 100-110$ are similar to the values measured by Guzmán et al. (2017) towards protoplanetary discs in HCN, and they are also consistent with the low values measured in pristine Solar system materials. However, N-fractionation

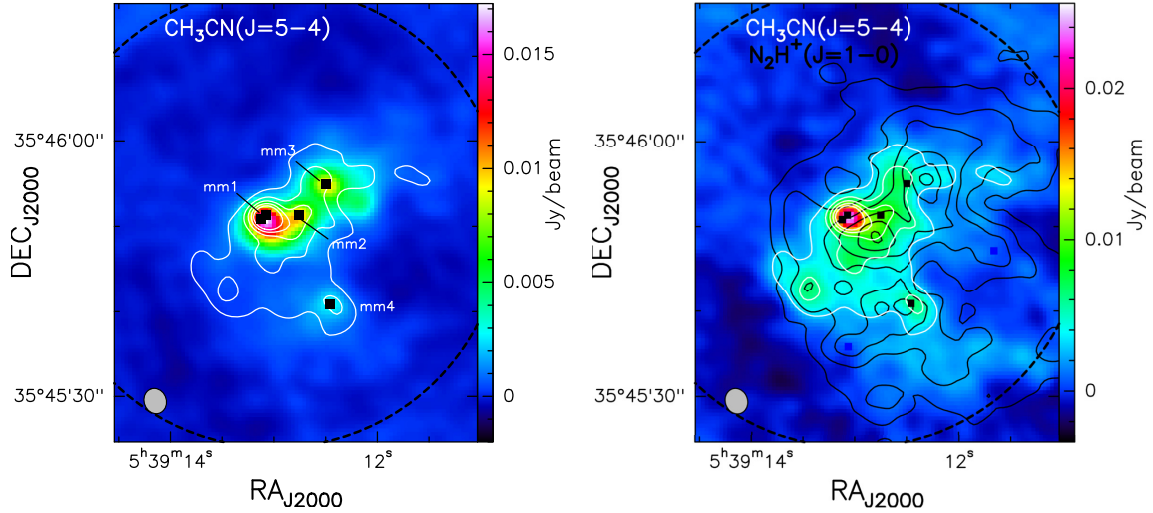


Figure 6. *Left-hand panel:* The colours are the 3mm-continuum intensity (the same as Fig. 1). The white contour levels are 5, 10, 15, 20, and 25 times the 1σ rms of the $\text{CH}_3\text{CN}(5-4)$ map, equal to $\sim 5 \times 0.6 \text{ mJy beam}^{-1}$. *Right-hand panel:* The colours are the averaged emission of $\text{CH}_3\text{CN}(5-4)$, the white contours are the same as in the left-hand panel, and the black contours are the same as in Fig. 2. In both panels the black squares indicate the positions of the continuum sources as in Fig. 2 (black). The dashed circle represents the NOEMA field of view and the synthesized beam is the ellipse indicated in the lower left corner.

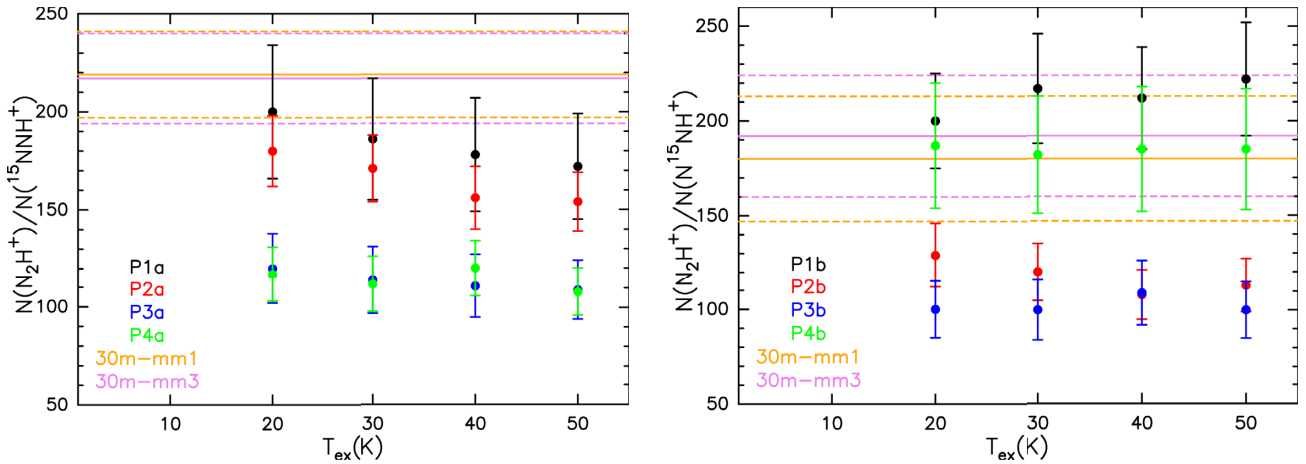


Figure 7. *Left-hand panel:* $^{14}\text{N}/^{15}\text{N}$ ratios obtained from $^{15}\text{NNH}^+$, as a function of the different T_{ex} assumed, towards P1a (black points), P2a (red points), P3a (blue points) and P4a (green points). *Right panel:* The same as the left panel but for N^{15}NH^+ towards P1b (black points), P2b (red points), P3b (blue points), and P4b (green points). In both panels the orange solid line is the value obtained in a polygon equal to the IRAM-30m beam towards mm1 (the dashed lines correspond to the error bar) and the pink dashed line is the same but towards mm3, for $^{15}\text{NNH}^+$ in the left-hand panel and N^{15}NH^+ in the right-hand panel. The T_{ex} assumed to compute the $^{14}\text{N}/^{15}\text{N}$ ratios toward 30m-mm1 and 30m-mm3 are equal to those derived in Fontani et al. (2015): 43 K for mm1 and 18 K for mm3.

of different molecules, like HCN and N_2H^+ , could be different. To investigate this point better, consistent measurements of N-fractionation from different species in the same sources are needed to understand the puzzle of nitrogen isotopic ratios. Moreover, high-mass angular resolution observations towards other high-mass star-forming regions are needed in order to confirm these results. In fact, it is also important to gather more data in sources that are good candidates to represent the environment in which our Sun was born. In this respect, intermediate- and high-mass star-forming cores are interesting targets because the Sun was probably born in a rich cluster that also contained massive stars (e.g. Adams 2010; Lichtenberg et al. 2019).

Unfortunately, none of the published chemical models up to now are able to reproduce the low $^{14}\text{N}/^{15}\text{N}$ observed in this work.

Moreover, they are not able to reproduce observed values of N-fractionation in N_2H^+ in general. However, they are gas-phase exchange models that feature only low-temperature exchange reactions as the only fractionation mechanism (e.g. Roueff et al. 2015; Wirström & Charnley 2018). Probably other mechanisms must be taken into account, like the isotope-selective photodissociation of N_2 and grain surface chemistry (Furuya & Aikawa et al. 2018). In particular, these authors have proposed some mechanisms to explain the ^{15}N depletion in N_2H^+ in pre-stellar cores starting from their parental clouds. They found that during the evolution of a molecular cloud, where the external UV radiation field is not fully shielded, the $^{14}\text{N}^{15}\text{N}$ molecule could be photodissociated where the $^{14}\text{N}_2$ is not, causing an enrichment of atomic ^{15}N . The subsequent adsorption of atomic N creates an enrichment of ^{15}N in NH_3 ice by surface

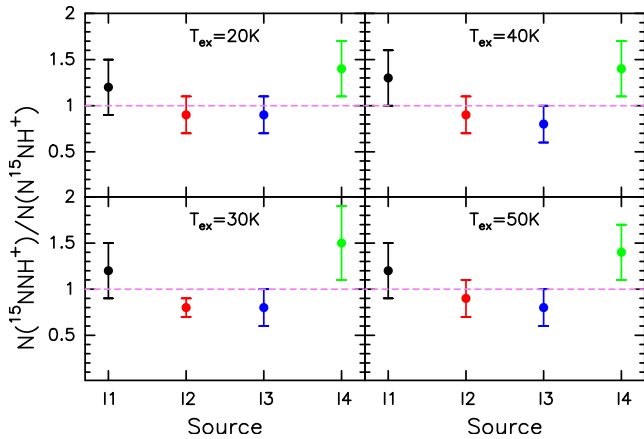


Figure 8. $^{15}\text{NNH}^+/\text{N}^{15}\text{NH}^+$ ratios towards I1 (black points), I2 (red points), I3 (blue points), and I4 (green points). Different panels show the results with the different T_{ex} assumed. The pink solid line represents the locus of points where $^{15}\text{NNH}^+/\text{N}^{15}\text{NH}^+ = 1$.

reactions. They found that as long as the photodesorption of NH_3 ice is less efficient than that of N_2 ice, the net effect is the loss of ^{15}N from the gas phase. However, these results are based on a specific physical model adapted for a cloud with a density of $\sim 10^4 \text{ cm}^{-3}$, which could not be appropriate for dense sources. To understand the existing ^{15}N observations, more numerical studies of ^{15}N -fractionation are needed.

4.3 $^{15}\text{NNH}^+$ versus N^{15}NH^+

In this section we will discuss about the possible differences between the two ^{15}N isotopologues of N_2H^+ : $^{15}\text{NNH}^+$ and N^{15}NH^+ . In order to do that, we have compared the $^{14}\text{N}/^{15}\text{N}$ ratios obtained from $^{15}\text{NNH}^+$ and N^{15}NH^+ towards I1, I2, I3, and I4, since the column densities of the two ^{15}N isotopologues were derived from the same regions.

In Fig. 8 the $^{15}\text{NNH}^+/\text{N}^{15}\text{NH}^+$ column density ratios, for the different excitation temperatures assumed, are shown. In this case, the dependence on the T_{ex} is small because both the ^{15}N -isotopologues are almost optically thin. We have found that $^{15}\text{NNH}^+$ is more abundant (at the 1σ level) with respect to N^{15}NH^+ towards I4, and the contrary towards I1, I2, and I3. Concerning what happens towards I4, it is difficult to interpret our results from an evolutionary point of view, because the nature of this source is unknown (as already mentioned in Section 4.1). In this case, the ratio between the two ^{15}N isotopologues is higher than one, also including the errorbar. This could be a clue that in some particular cases of densities and temperatures the two ^{15}N isotopologues could form through different reaction pathways. This finding should also be confirmed by a higher statistics.

As already mentioned, the most recent chemical models are not able to reproduce a different behaviour between the two ^{15}N isotopologues. Other works towards very different environments show a tentative trend of $^{15}\text{NNH}^+$ to be less abundant than N^{15}NH^+ : Kahane et al. (2018) towards OMC-2 FIR4 ($^{15}\text{NNH}^+/\text{N}^{15}\text{NH}^+ \sim 0.8$) and Redaelli et al. (2018) towards the pre-stellar cores L1544 and L694-2 ($^{15}\text{NNH}^+/\text{N}^{15}\text{NH}^+ \sim 0.9$ and ~ 0.8 , respectively).

4.4 $^{14}\text{N}/^{15}\text{N}$ ratios in diffuse regions

In Table 6 the results obtained towards the more diffuse N_2H^+ emission regions D1, D2, and D3 are shown. All of these results are lower limits since the ^{15}N isotopologues were not detected, except for $^{15}\text{NNH}^+$ towards D2. The lower limit values obtained are, on average, higher than 200–250. These are also the maximum values obtained towards the peak-emission regions. Only the lower limits towards D2 from N^{15}NH^+ are smaller, but given that the detections from $^{15}\text{NNH}^+$ confirm a $^{14}\text{N}/^{15}\text{N}$ ratio of ~ 320 , and that we have found a maximum difference of ~ 1.5 (see previous section), we can confirm that this lower limit corresponds to $^{14}\text{N}/^{15}\text{N}$ ratios higher than 200. These results mean that ^{15}N tend to be less enriched in N_2H^+ in the outer parts of a star-forming region. This could be a possible confirmation of the work of Furuya et al. (2018): In NI/N_2 transition zones, where the gas is less dense and the interstellar UV radiation field is not significantly attenuated ($A_V < 3 \text{ mag}$), the ^{15}N is frozen in NH_3 ice and there is a loss of ^{15}N from the gas phase.

5 CONCLUSION

We used the IRAM NOEMA Interferometer to observe the emission of $\text{N}_2\text{H}^+(1-0)$ and its ^{15}N isotopologues towards the high-mass star-forming protocluster IRAS 05358+3543. The N_2H^+ dense gas emission consists of three main cores, two of which are displaced with respect to the 3mm continuum sources, probably because of the star formation activity that causes the N_2H^+ destruction by CO desorption from grain mantles. We have also discussed the presence of two other N_2H^+ -emission zones: A and B. The first defines a fourth core from the ^{15}N isotopologue emission maps and corresponds to a H^{13}CO^+ peak observed in previous works. The second is probably associated with an outflow coming out from the more evolved region in the north.

The $^{14}\text{N}/^{15}\text{N}$ ratios derived towards regions that correspond to the IRAM-30m beam are higher than those from the cores of the cluster. This indicates the possibility that ^{15}N enrichment in star-forming regions is a local effect. The lower values of ~ 100 towards the cores are similar to some values measured in protoplanetary discs, and also to the low values measured in the pristine Solar system material. Moreover, the $^{14}\text{N}/^{15}\text{N}$ ratios derived from $^{15}\text{NNH}^+$ and N^{15}NH^+ show some differences. In particular, towards I1 and I4 $^{15}\text{NNH}^+$ is more abundant than N^{15}NH^+ . However, the most recent chemical models are not able to reproduce the low $^{14}\text{N}/^{15}\text{N}$ values found for N_2H^+ in this work and in other works.

Finally, the $^{14}\text{N}/^{15}\text{N}$ lower limits derived in the more diffuse N_2H^+ emission regions of the cluster point to values higher than those derived in the cores. This confirms the conclusion that N-fractionation, measured from N_2H^+ , seems to be a local effect, at least in this high-mass star-forming region. However, more observations, also of different molecules, are needed to unveil which physical parameters are affecting the N-fractionation, thus helping us to gain understanding of the chemistry involved.

ACKNOWLEDGEMENTS

This work is based on observations carried out under projects number S16AK and 081-16 with the IRAM NOEMA Interferometer and 30m telescope, respectively. IRAM is supported by INSU/CNRS (France), MPG (Germany), and IGN (Spain). We are grateful to the IRAM NOEMA staff for their help during the calibration of the data and the IRAM-30m telescope staff for

their help during the observations. Many thanks to the anonymous referee for the careful reading of the paper and the comments that improved the work. LC acknowledges support from the Italian Ministero dell'Istruzione, Università e Ricerca through the grant Progetti Premiali 2012 - iALMA (CUP C52I13000140001). PC acknowledges support from the European Research Council (project PALs 320620). LC sincerely acknowledges the hospitality of the Joint ALMA Observatory (JAO), where a significant part of the manuscript was written.

REFERENCES

- Adams F. C., 2010, *ARA&A*, 48, 47
- Beuther H., Schilke P., Gueth F., McCaughrean M., Andersen M., Sridharan T. K., Menten K. M., 2002a, *A&A*, 387, 931
- Beuther H., Schilke P., Menten K. M., Motte F., Sridharan T. K., Wyrowski F., 2002b, *ApJ*, 566, 945
- Beuther H., Schilke P., Sridharan T. K., Menten K. M., Walmsley C. M., Wyrowski F., 2002c, *A&A*, 383, 892
- Beuther H., Walsh A., Schilke P., Sridharan T. K., Menten K. M., Wyrowski F., 2002d, *A&A*, 390, 289
- Beuther H., Leurini S., Schilke P., Wyrowski F., Menten K. M., Zhang Q., 2007a, *A&A*, 466, 1065
- Bizzocchi L., Caselli P., Leonardo E., Dore L., 2013, *A&A*, 555, AA109
- Busquet G., Estalella R., Zhang Q., Viti S., Palau A., Ho P. T. P., Sánchez-Monge Á., 2011, *A&A*, 525, A141
- Cazzoli G., Puzzarini C., 2006, *J. Mol. Spectrosc.*, 240, 153
- Cazzoli G., Cludi L., Buffa G., Puzzarini C., 2012, *ApJS*, 203, 11
- Codella C. et al., 2013, *ApJ*, 776, 52
- Colzi L., Fontani F., Caselli P., Ceccarelli C., Hily-Blant P., Bizzocchi L., 2018a, *A&A*, 609, A129
- Colzi L., Fontani F., Rivilla V. M., Sánchez-Monge A., Testi L., Beltrán M. T., Caselli P., 2018b, *MNRAS*, 478, 3693
- Daniel F. et al., 2016, *A&A*, 592, A45
- Di Francesco J., André P., Myers P. C., 2004, *ApJ*, 617, 425
- Dore L., Bizzocchi L., Degli Esposti C., Tinti F., 2009, *A&A*, 496, 275
- Endres C. P., Schlemmer S., Schilke P., Stutzki J., Müller H. S. P., 2016, *J. Mol. Spectrosc.*, 327, 95
- Fontani F., Caselli P., Palau A., Bizzocchi L., Ceccarelli C., 2015, *ApJ*, 808, L46
- Fontani F., Vagnoli A., Padovani M., Colzi L., Caselli P., Rivilla V. M., 2018, *MNRAS*, 481, L79
- Furuya K., Aikawa Y., 2018, *ApJ*, 857, 105
- Georgelin Y. M., 1975, PhD thesis, Univ. Provence, Observatoire de Marseille
- Gerin M. et al., 2009, *A&A*, 498, L9
- Ginsburg A. G., Bally J., Yan C., Williams J. P., 2009, *ApJ*, 707, 1
- Guzmán V. V., Öberg K. I., Huang J., Loomis R., Qi C., 2017, *ApJ*, 836, 30
- Heays A. N., Visser R., Gredel R., Ubachs W., Lewis B. R., Gibson S. T., van Dishoeck E. F., 2014, *A&A*, 562, A61
- Heyer, Carpenter J. M., Ladd E. F., 1996, *ApJ*, 463, 630
- Hily-Blant P., Pineau des Forêts G., Faure A., Le Gal R., Padovani M., 2013, *A&A*, 557, A65
- Hily-Blant P., Magalhães V., Kastner J., Faure A., Forveille T., Qi C., 2017, *A&A*, 603, L6
- Hu B. et al., 2016, *ApJ*, 833, 9
- Kahane C., Al-Edhari A. J., Ceccarelli C., Lopez-Sepulcre A., Fontani F., Mihkel K., 2018, *ApJ*, 825, 130
- Lang K. R., Mitton J., 1992, *Journal of the British Astronomical Association*, 102, 226
- Lee C., Ho P. T. P., White S. M., 2005, *ApJ*, 619, 948
- Leurini S., Beuther H., Schilke P., Wyrowski F., Zhang Q., Menten K. M., 2007, *A&A*, 475, 3
- Leurini S. et al., 2011, *A&A*, 533, A85
- Lichtenberg T. et al., 2019, *Nat. Astron*
- Loison J.-C., Wakelam V., Gratier P., Hickson K. M., 2019, *MNRAS*, 484, 2747
- Lu X., Zhang Q., Liu H. Ba., Wang J., Gu Q., 2014, *ApJ*, 790, 2
- Magalhães V. S., Hily-Blant P., Faure A., Hernandez-Vera M., Lique F., 2018, *A&A*, 615, A52
- Marty B., Zimmermann L., Burnard P. G., 2009, *Geochim. Cosmochim. Acta*, 73, 842
- Marty B. et al., 2010, *Geochim. Cosmochim. Acta*, 74, 340
- McGeoch M. W., Samoril T., Zapotok D., McGeoch J. E. M., 2018, preprint ([arXiv:1811.06578](https://arxiv.org/abs/1811.06578))
- Minier V., Booth R. S., Conway J. E., 2000, *A&A*, 362, 1093
- Mininni C., Fontani F., Rivilla V. M., Beltrán M. T., Caselli P., Vasyunin A., 2018, *MNRAS*, 476, L39
- Müller H. S. P., Thorwirth S., Roth D. A., Winnewisser G., 2001, *A&A*, 370, L49
- Müller H. S. P., Schöder F., Stutzki J., Winnewisser G., 2005, *J. Mol. Struct.*, 742, 215
- Redaelli E., Bizzocchi L., Caselli P., Harju J., Chacón-Tanarro A., Leonardo E., Dore L., 2018, *A&A*, 617, A7
- Reid M. A., Matthews B. C., 2008, *ApJ*, 675, 1343
- Rivilla V. M., Fontani F., Beltrán M. T., Vasyunin A., Caselli P., Martín-Pintado J., Cesaroni R., 2016, *ApJ*, 826, 161
- Rivilla V. M., Beltrán M. T., Cesaroni R., Fontani F., Codella C., Zhang Q., 2017, *A&A*, 598, A59
- Rivilla V. M., Beltrán M. T., Vasyunin A., Caselli P., Viti S., Fontani F., Cesaroni R., 2019, *MNRAS*, 483, 806
- Romano D., Matteucci F., Zhang Z.-Y., Papadopoulos P. P., Ivison R. J., 2017, *MNRAS*, 470, 401
- Roueff E., Loison J. C., Hickson K. M., 2015, *A&A*, 576, A99
- Snell R. L., Dickman R. L., Huang Y.-L., 1990, *ApJ*, 352, 139
- Sridharan T. K., Beuther H., Schilke P., Menten K. M., Wyrowski F., 2002, *ApJ*, 566, 931
- Terzieva R., Herbst E., 2000, *MNRAS*, 317, 563
- van Kooten E. M. M. E., Nagashima K., Kasama T., Wampfler S. F., Ramsey J. P. et al., 2017, *Geochim. Cosmochim. Acta*, 205, 119
- Visser R., Bruderer S., Cazzoletti P., Facchini S., Heays A. N., van Dishoeck E. F., 2018, *A&A*, 615, A75
- Wampfler S. F., Jørgensen J. K., Bizzarro M., Bisschop S. E., 2014, *A&A*, 572, A24
- Wirström E. S., Charnley S. B., 2018, *MNRAS*, 474, 3
- Wirström E. S., Adande G., Milam S. N., Charnley S. B., Cordiner M. A., 2016, *IAU Focus Meeting*, 29, 271
- Yang B. et al., 2017, *A&A*, 609, L4
- Zeng S. et al., 2017, *A&A*, 603, A22

APPENDIX A: EXTRACTED SPECTRA

In this appendix, the extracted spectra of the $J = 1-0$ transition of N_2H^+ , $^{15}NNH^+$, and $N^{15}NH^+$ from the regions P1a–P4a, P1b–P4b, I1, I2, I3, I4, D1, D2, and D3 are shown. The definition of the regions can be found in Section 3.

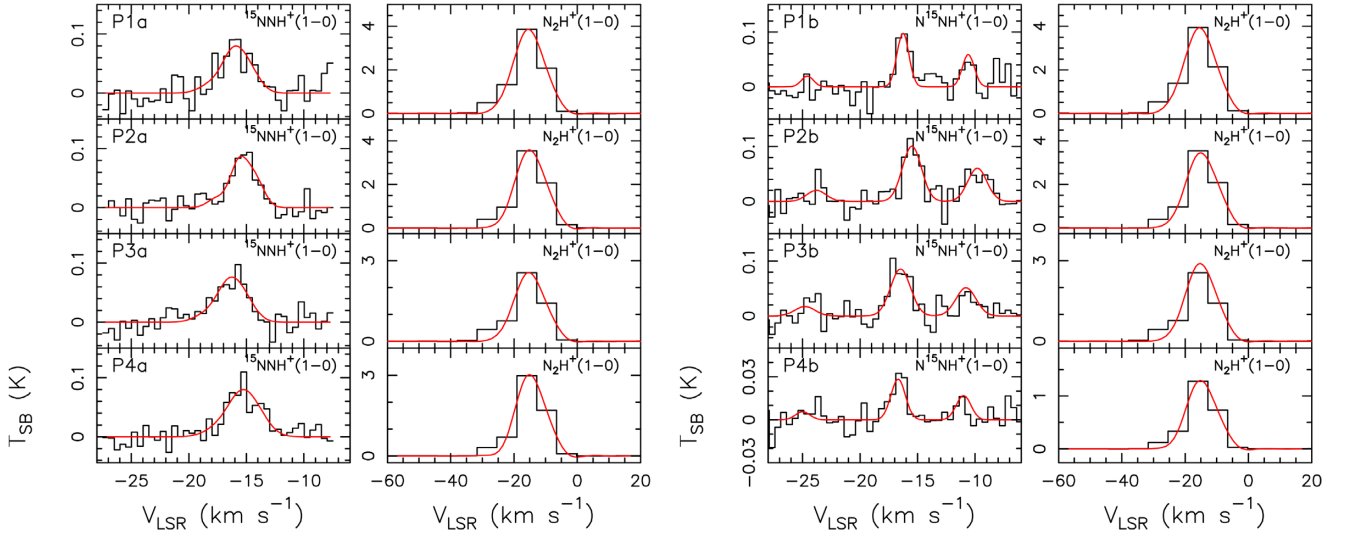


Figure A1. Left-hand panel: spectra of the $^{15}\text{NNH}^+(1-0)$ and $\text{N}_2\text{H}^+(1-0)$ transitions (first and second column, respectively) obtained for the P1a, P2a, P3a, and P4a regions (first, second, third, and fourth line, respectively). Right-hand panel: spectra of the $\text{N}^{15}\text{NH}^+(1-0)$ and $\text{N}_2\text{H}^+(1-0)$ transitions (first and second column, respectively) obtained for the P1b, P2b, P3b, and P4b regions (first, second, third, and fourth line, respectively). For each spectrum, in both panels, the x -axis represents the systematic velocity of the source. The y -axis shows the intensity in synthesized beam temperature units. The red curves are the best Gaussian fits obtained with MADCUBA with a $T_{\text{ex}} = 30$ K.

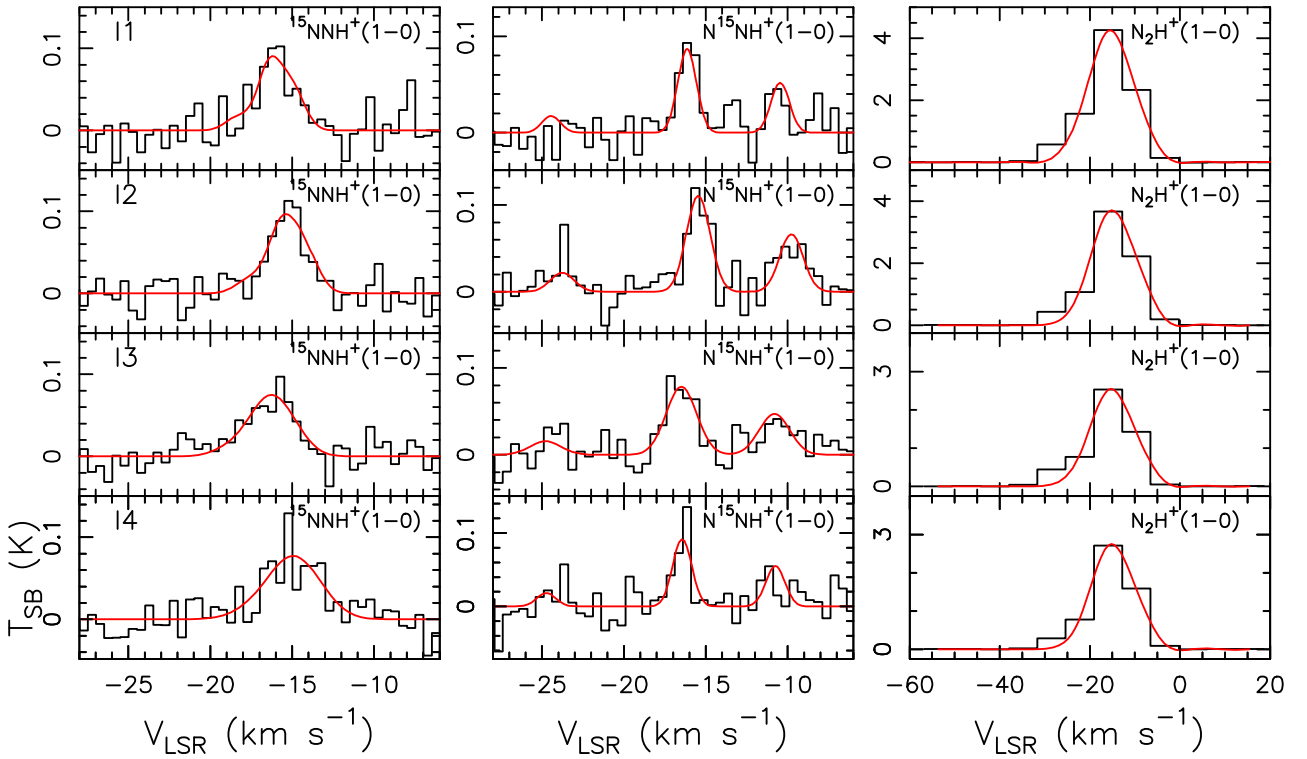


Figure A2. Spectra of the $^{15}\text{NNH}^+(1-0)$, $\text{N}^{15}\text{NH}^+(1-0)$, and $\text{N}_2\text{H}^+(1-0)$ transitions (first, second, and third column, respectively) obtained for the I1, I2, I3, and I4 regions (first, second, third, and fourth line, respectively). For each spectrum the x -axis represents the systematic velocity of the source. The y -axis shows the intensity in synthesized beam temperature units. The red curves are the best Gaussian fits obtained with MADCUBA with a $T_{\text{ex}} = 30$ K.

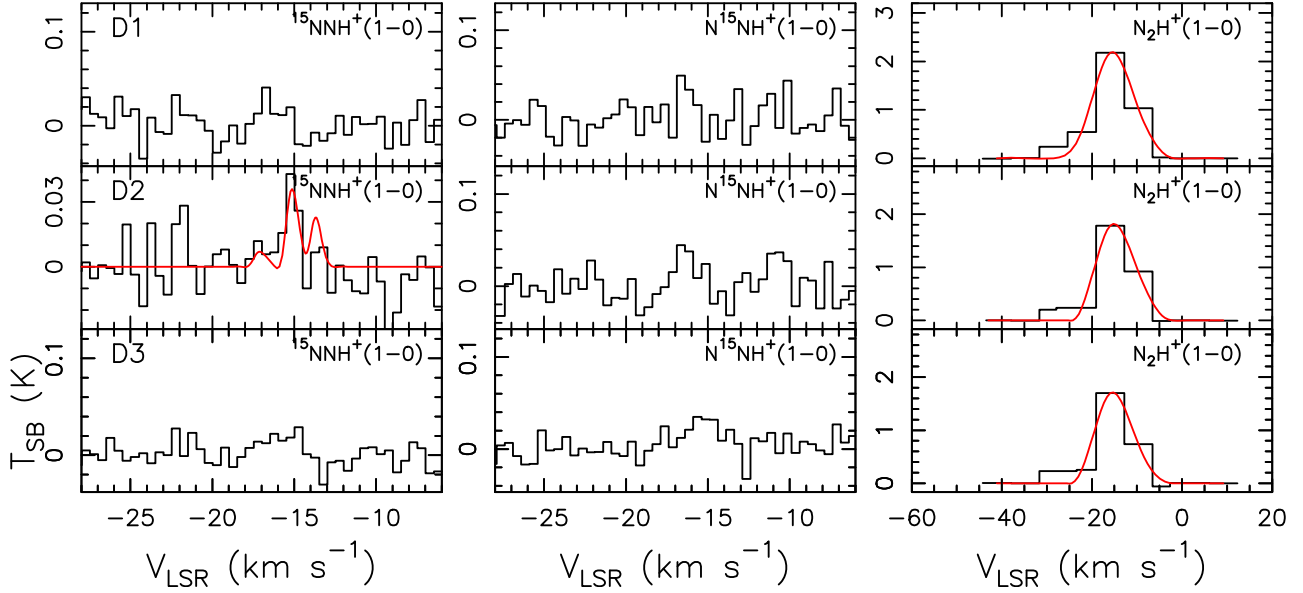


Figure A3. Spectra of the $^{15}\text{NNH}^+(1-0)$, $\text{N}^{15}\text{NH}^+(1-0)$, and $\text{N}_2\text{H}^+(1-0)$ transitions (first, second, and third column, respectively) obtained for the D1, D2, and D3 regions (first, and third line, respectively). For each spectrum the x-axis represents the systematic velocity of the source. The y-axis shows the intensity in synthesized beam temperature units. The red curves are the best Gaussian fits obtained with MADCUBA with a $T_{\text{ex}} = 30$ K.

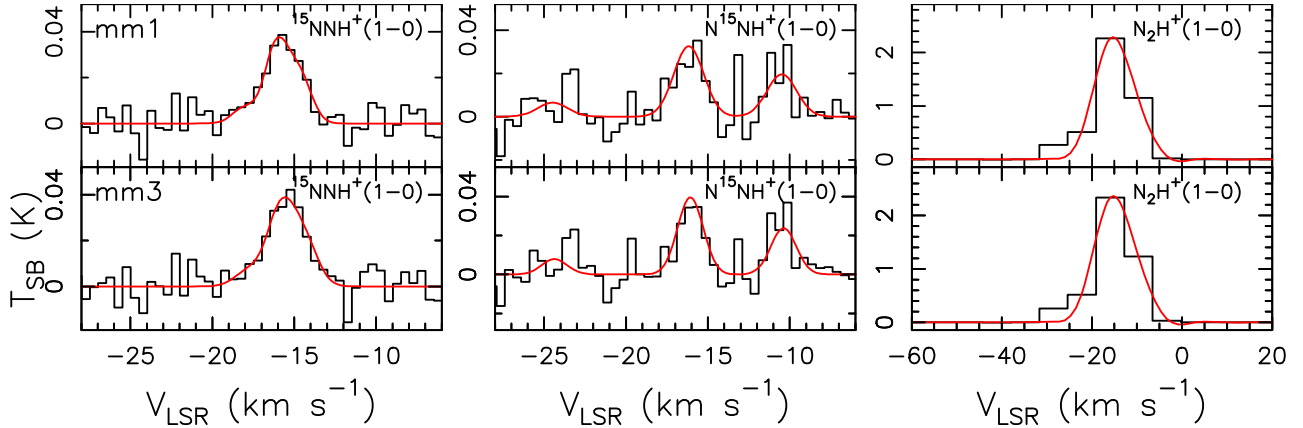


Figure A4. Spectra of the $^{15}\text{NNH}^+(1-0)$, $\text{N}^{15}\text{NH}^+(1-0)$, and $\text{N}_2\text{H}^+(1-0)$ transitions (first, second, and third column, respectively) obtained for the regions that correspond to the IRAM-30m beam around mm1 and mm3 (first and second line, respectively). For each spectrum the x-axis represents the systematic velocity of the source. The y-axis shows the intensity in synthesized beam temperature units. The red curves are the best Gaussian fits obtained with MADCUBA with a $T_{\text{ex}} = 43$ K for mm1 and a $T_{\text{ex}} = 18$ K for mm3, which are equal to those derived in Fontani et al. (2015).

APPENDIX B: SPECTRA SIMULATION TESTS

In this appendix, we have estimated how much our results are influenced by the different spectral resolution between the main isotopologue (N_2H^+ , of about 6.45 km s^{-1}) and the ^{15}N isotopologues ($^{15}\text{NNH}^+$ and N^{15}NH^+ , of about 0.5 km s^{-1}). For this test we have taken into account the spectra extracted from P1a and P1b, and the corresponding fit results with a $T_{\text{ex}} = 20$ K.

B1 ^{15}N isotopologues at lower spectral resolution

We have smoothed the $^{15}\text{NNH}^+(1-0)$ transition to a 6.5 km s^{-1} resolution. In Fig. B1, the black spectrum is the observed one, the blue solid line is the fit to the observed spectrum, and the red line is the smoothed one. The integrated intensity ($A = \int T_{\text{MB}} dv$) of the observed spectrum is $(0.27 \pm 0.04) \text{ K km s}^{-1}$ (relative error $\Delta A/A \simeq$

15 per cent), while the integrated intensity of the smoothed spectrum is $(0.31 \pm 0.06) \text{ K km s}^{-1}$, 13 per cent higher than the observed one. This error is comparable to the error given from the fit. We have done the same analysis with $\text{N}^{15}\text{NH}^+(1-0)$ (Fig. B2), for which we have obtained, for the smoothed spectrum, an integrated intensity of $(0.26 \pm 0.08) \text{ K km s}^{-1}$, 12 per cent higher than the observed one $(0.23 \pm 0.03 \text{ K km s}^{-1})$, which again is comparable with the relative error given by the fit of the observed spectrum ($\Delta A/A \simeq 13$ per cent). The test hence shows that the integrated intensity of the ^{15}N isotopologues, and thus their column densities, is not affected by changing the resolution from 0.5 to 6.5 km s^{-1} .

B2 N_2H^+ at higher spectral resolution

We have simulated the spectrum of $\text{N}_2\text{H}^+(1-0)$ with a resolution of 0.5 km s^{-1} using the results of the fit obtained for a $T_{\text{ex}} = 20$ K,

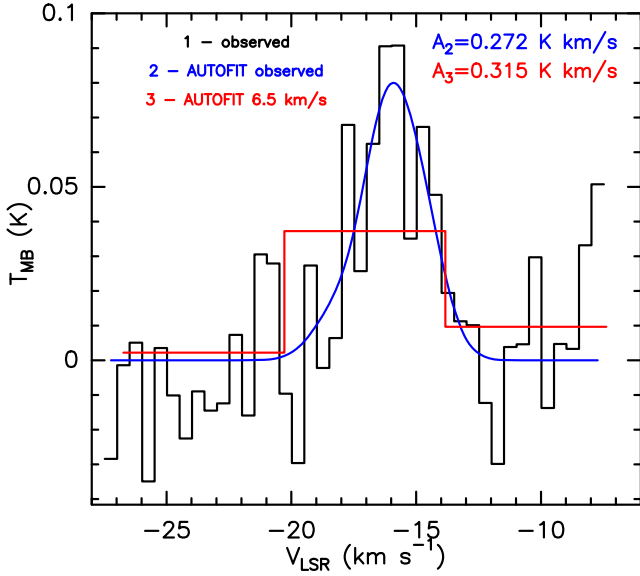


Figure B1. $^{15}\text{NNH}^+(1-0)$ spectra. The observed spectrum is the black one, the best fit to the observed spectrum is the blue solid line, and the smoothed spectrum to 6.5 km s^{-1} is the red one.

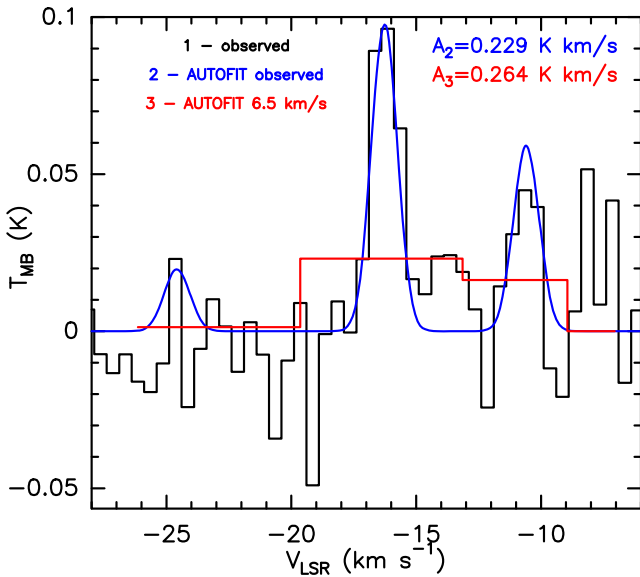


Figure B2. $\text{N}^{15}\text{NH}^+(1-0)$ spectra. The observed spectrum is the black one, the best fit to the observed spectrum is the blue solid line, and the smoothed spectrum to 6.5 km s^{-1} is the red one.

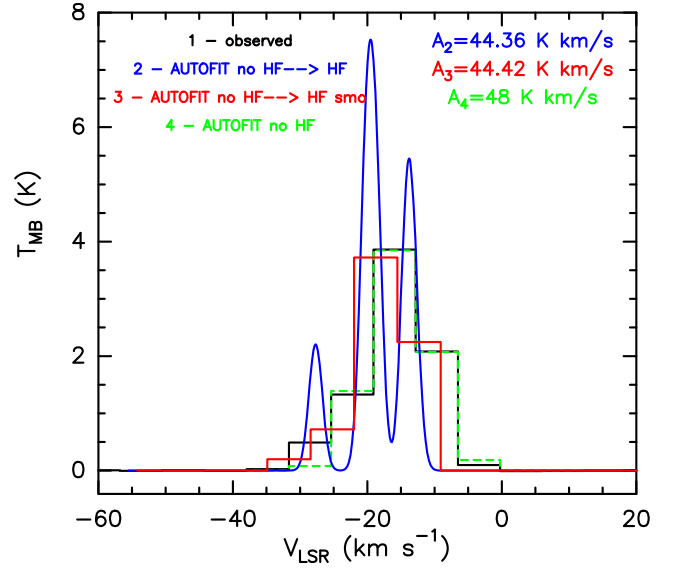


Figure B3. $\text{N}_2\text{H}^+(1-0)$ spectra. The observed spectrum is the black one and the best fit to this is the green dashed line. The blue solid line is the simulated spectrum at high spectral resolution (0.5 km s^{-1}) with a line width of 2.3 km s^{-1} and the red one is the smooth of the simulation to 6.5 km s^{-1} .

towards P1a, but with a line width of 2.3 km s^{-1} (which is the average value measured from $^{15}\text{NNH}^+$). The obtained spectrum is the blue in Fig. B3, with an integrated intensity of $(44 \pm 2) \text{ K km s}^{-1}$. Then, we have smoothed this simulated spectrum to 6.45 km s^{-1} , obtaining the red one in the same figure. The integrated intensity of this latter is the same of that at higher spectral resolution. We can also note that the smoothed simulated spectrum is comparable with the observed one (black) that has an integrated intensity of $(48 \pm 2) \text{ K km s}^{-1}$ ($\Delta A/A \simeq 4$ per cent), 8 per cent higher than the simulated one. We can conclude that, even if we cannot resolve the hyperfine structure of $\text{N}_2\text{H}^+(1-0)$, with our analysis we have obtained an accurate integrated intensity, with at most 4 per cent overestimation.

APPENDIX C: FIT RESULTS

In this appendix is shown the results of the fitting procedure to the $\text{N}_2\text{H}^+(1-0)$, $^{15}\text{NNH}^+(1-0)$, and $\text{N}^{15}\text{NH}^+(1-0)$ transitions towards all the sources defined in Section 3. The method is explained in Section 3.3.

Table C1. Values obtained with the fitting procedure described in Section 3.3 to the $J = 1-0$ transition of N_2H^+ and $^{15}\text{NNH}^+$ towards P1a, P2a, P3a, and P4a (top panel of the table), and of the $J = 1-0$ transition of N_2H^+ and N^{15}NH^+ towards P1b, P1b, P3b, and P4b (bottom panel of the table).

Source	$\text{N}_2\text{H}^+(1-0)$					$^{15}\text{NNH}^+(1-0)$				
	T_{ex} (K)	FWHM ^a (km s ⁻¹)	v_{LSR} (km s ⁻¹)	τ	N_{tot} ($\times 10^{14}$ cm ⁻²)	T_{ex} (K)	FWHM (km s ⁻¹)	v_{LSR} (km s ⁻¹)	τ^b	N_{tot} ($\times 10^{11}$ cm ⁻²)
P1a	20	11.1 ± 0.6	-15.2 ± 0.3	0.26 ± 0.02	1.0 ± 0.1	20	2.2 ± 0.7	-16.2 ± 0.3	0.002 ± 0.001	5 ± 1
	30	11.3 ± 0.6	-15.2 ± 0.3	0.16 ± 0.02	1.3 ± 0.2	30	2.2 ± 0.7	-16.2 ± 0.3	0.002 ± 0.001	7 ± 2
	40	11.3 ± 0.6	-15.2 ± 0.3	0.112 ± 0.008	1.6 ± 0.2	40	2.3 ± 0.7	-16.2 ± 0.3	0.002 ± 0.001	9 ± 2
	50	11.4 ± 0.6	-15.2 ± 0.3	0.087 ± 0.006	1.9 ± 0.3	50	2.3 ± 0.7	-16.2 ± 0.3	0.0013 ± 0.0005	11 ± 3
P2a	20	10.6 ± 0.7	-14.7 ± 0.3	0.25 ± 0.02	0.9 ± 0.1	20	1.8 ± 0.3	-15.6 ± 0.1	0.0027 ± 0.0005	5 ± 1
	30	10.8 ± 0.7	-14.7 ± 0.3	0.15 ± 0.02	1.2 ± 0.2	30	1.8 ± 0.3	-15.6 ± 0.1	0.0017 ± 0.0003	7 ± 1
	40	10.9 ± 0.7	-14.7 ± 0.3	0.105 ± 0.008	1.4 ± 0.2	40	1.8 ± 0.3	-15.6 ± 0.1	0.0013 ± 0.0003	9 ± 2
	50	10.9 ± 0.7	-14.7 ± 0.3	0.082 ± 0.006	1.7 ± 0.3	50	1.8 ± 0.3	-15.6 ± 0.1	0.0010 ± 0.0002	11 ± 2
P3a	20	11 ± 1	-15.0 ± 0.5	0.17 ± 0.02	0.6 ± 0.1	20	2.3 ± 0.6	-16.6 ± 0.2	0.002 ± 0.001	5 ± 1
	30	11 ± 1	-15.0 ± 0.5	0.10 ± 0.02	0.8 ± 0.1	30	2.3 ± 0.6	-16.6 ± 0.2	0.0013 ± 0.0003	7 ± 1
	40	11 ± 1	-15.0 ± 0.5	0.073 ± 0.009	1.0 ± 0.2	40	2.3 ± 0.6	-16.6 ± 0.2	0.0010 ± 0.0002	9 ± 2
	50	11 ± 1	-15.0 ± 0.5	0.057 ± 0.007	1.2 ± 0.2	50	2.3 ± 0.6	-16.6 ± 0.2	0.0008 ± 0.0002	11 ± 2
P4a	20	10.2 ± 0.6	-14.6 ± 0.3	0.20 ± 0.02	0.7 ± 0.1	20	2.7 ± 0.6	-15.6 ± 0.2	0.0021 ± 0.0005	6 ± 1
	30	10.3 ± 0.6	-14.6 ± 0.3	0.12 ± 0.01	0.9 ± 0.1	30	2.7 ± 0.6	-15.6 ± 0.2	0.0013 ± 0.0003	8 ± 2
	40	10.3 ± 0.6	-14.6 ± 0.3	0.089 ± 0.007	1.2 ± 0.2	40	2.7 ± 0.6	-15.6 ± 0.2	0.0009 ± 0.0002	10 ± 2
	50	10.4 ± 0.6	-14.6 ± 0.3	0.069 ± 0.005	1.4 ± 0.2	50	2.7 ± 0.6	-15.6 ± 0.2	0.0007 ± 0.0002	13 ± 3

Source	$\text{N}_2\text{H}^+(1-0)$					$\text{N}^{15}\text{NH}^+(1-0)$				
	T_{ex} (K)	FWHM ^a (km s ⁻¹)	v_{LSR} (km s ⁻¹)	τ	N_{tot} ($\times 10^{14}$ cm ⁻²)	T_{ex} (K)	FWHM (km s ⁻¹)	v_{LSR} (km s ⁻¹)	τ^b	N_{tot} ($\times 10^{11}$ cm ⁻²)
P1b	20	11.2 ± 0.7	-15.2 ± 0.3	0.27 ± 0.02	1.0 ± 0.2	20	1.2 ± 0.2	-16.27 ± 0.07	0.004 ± 0.001	5 ± 1
	30	11.4 ± 0.7	-15.2 ± 0.3	0.16 ± 0.02	1.3 ± 0.2	30	1.2 ± 0.2	-16.27 ± 0.07	0.0022 ± 0.0004	6 ± 1
	40	11.5 ± 0.7	-15.2 ± 0.3	0.114 ± 0.009	1.7 ± 0.3	40	1.2 ± 0.2	-16.27 ± 0.07	0.0016 ± 0.0003	8 ± 2
	50	11.5 ± 0.7	-15.2 ± 0.3	0.089 ± 0.007	2.0 ± 0.3	50	1.2 ± 0.2	-16.27 ± 0.07	0.0013 ± 0.0002	9 ± 2
P2b	20	11.0 ± 0.7	-14.7 ± 0.3	0.23 ± 0.02	0.9 ± 0.1	20	1.9 ± 0.3	-15.5 ± 0.1	0.004 ± 0.001	7 ± 2
	30	11.1 ± 0.6	-14.7 ± 0.3	0.14 ± 0.01	1.2 ± 0.2	30	1.9 ± 0.3	-15.5 ± 0.1	0.0023 ± 0.0004	10 ± 2
	40	11.2 ± 0.6	-14.7 ± 0.3	0.110 ± 0.007	1.4 ± 0.2	40	1.9 ± 0.3	-15.5 ± 0.1	0.0016 ± 0.0003	13 ± 3
	50	11.2 ± 0.6	-14.7 ± 0.3	0.078 ± 0.006	1.7 ± 0.3	50	1.9 ± 0.3	-15.5 ± 0.1	0.0013 ± 0.0002	15 ± 3
P3b	20	11 ± 1	-14.9 ± 0.5	0.20 ± 0.03	0.7 ± 0.1	20	2.0 ± 0.3	-16.5 ± 0.2	0.003 ± 0.001	7 ± 1
	30	11 ± 1	-14.9 ± 0.5	0.12 ± 0.02	0.9 ± 0.2	30	2.0 ± 0.3	-16.5 ± 0.2	0.0019 ± 0.0004	9 ± 2
	40	11 ± 1	-14.9 ± 0.5	0.08 ± 0.01	1.2 ± 0.2	40	2.0 ± 0.3	-16.5 ± 0.2	0.0014 ± 0.0003	11 ± 3
	50	11 ± 1	-14.9 ± 0.5	0.065 ± 0.008	1.4 ± 0.3	50	2.0 ± 0.3	-16.5 ± 0.2	0.0011 ± 0.0002	14 ± 3
P4b	20	10.7 ± 0.6	-14.7 ± 0.3	0.082 ± 0.006	0.30 ± 0.04	20	1.5 ± 0.3	-16.7 ± 0.2	0.0010 ± 0.0003	1.6 ± 0.4
	30	10.7 ± 0.6	-14.7 ± 0.3	0.051 ± 0.004	0.40 ± 0.06	30	1.5 ± 0.3	-16.7 ± 0.2	0.0006 ± 0.0002	2.2 ± 0.6
	40	10.7 ± 0.6	-14.7 ± 0.3	0.037 ± 0.003	0.50 ± 0.07	40	1.5 ± 0.3	-16.7 ± 0.2	0.0005 ± 0.0001	2.7 ± 0.7
	50	10.7 ± 0.6	-14.7 ± 0.3	0.029 ± 0.002	0.61 ± 0.09	50	1.5 ± 0.3	-16.7 ± 0.2	0.00040 ± 0.00009	3.3 ± 0.9

^aNote that these FWHM overestimate those obtained with the ^{15}N isotopologues since N_2H^+ has a spectral resolution higher than the physical FWHM.^bOpacity of the main hyperfine component.

Table C2. Values obtained with the fitting procedure described in Section 3.3 to the $N_2H^+(1-0)$, $^{15}NNH^+(1-0)$, and $N^{15}NH^+(1-0)$ transitions towards I1, I2, I3, and I4.

Source	$N_2H^+(1-0)$				
	T_{ex} (K)	FWHM ^a (km s ⁻¹)	v_{LSR} (km s ⁻¹)	τ	N_{tot} ($\times 10^{14}$ cm ⁻²)
I1	20	11.3 ± 0.7	-15.3 ± 0.3	0.29 ± 0.03	1.1 ± 0.2
	30	11.5 ± 0.7	-15.3 ± 0.3	0.17 ± 0.02	1.5 ± 0.2
	40	11.6 ± 0.7	-15.3 ± 0.3	0.124 ± 0.009	1.8 ± 0.3
	50	11.7 ± 0.7	-15.3 ± 0.3	0.096 ± 0.007	2.2 ± 0.3
I2	20	11.0 ± 0.6	-14.7 ± 0.3	0.25 ± 0.02	1.0 ± 0.2
	30	11.1 ± 0.7	-14.7 ± 0.3	0.15 ± 0.02	1.2 ± 0.2
	40	11.2 ± 0.7	-14.7 ± 0.3	0.109 ± 0.009	1.5 ± 0.3
	50	11.3 ± 0.7	-14.7 ± 0.3	0.084 ± 0.007	1.9 ± 0.3
I3	20	11.0 ± 0.9	-15.0 ± 0.5	0.17 ± 0.02	0.6 ± 0.1
	30	11.1 ± 0.9	-15.0 ± 0.5	0.10 ± 0.01	0.8 ± 0.2
	40	11.2 ± 0.9	-15.0 ± 0.5	0.073 ± 0.008	1.0 ± 0.2
	50	11.2 ± 0.9	-15.0 ± 0.5	0.057 ± 0.006	1.2 ± 0.2
I4	20	10.8 ± 0.6	-14.8 ± 0.3	0.18 ± 0.02	0.7 ± 0.1
	30	10.9 ± 0.6	-14.8 ± 0.3	0.111 ± 0.008	0.9 ± 0.1
	40	11.0 ± 0.6	-14.7 ± 0.3	0.079 ± 0.006	1.1 ± 0.2
	50	11.0 ± 0.6	-14.7 ± 0.3	0.062 ± 0.004	1.3 ± 0.2

Source	$^{15}NNH^+(1-0)$					$N^{15}NH^+(1-0)$				
	T_{ex} (K)	FWHM (km s ⁻¹)	v_{LSR} (km s ⁻¹)	τ^b	N_{tot} ($\times 10^{11}$ cm ⁻²)	T_{ex} (K)	FWHM (km s ⁻¹)	v_{LSR} (km s ⁻¹)	τ^b	N_{tot} ($\times 10^{11}$ cm ⁻²)
I1	20	1.7 ± 0.5	-16.4 ± 0.2	0.005 ± 0.001	5 ± 1	20	1.3 ± 0.3	-16.1 ± 0.1	0.005 ± 0.001	4 ± 1
	30	1.7 ± 0.5	-16.4 ± 0.2	0.002 ± 0.001	7 ± 2	30	1.3 ± 0.3	-16.1 ± 0.1	0.003 ± 0.001	6 ± 2
	40	1.7 ± 0.5	-16.4 ± 0.2	0.002 ± 0.001	9 ± 2	40	1.3 ± 0.3	-16.1 ± 0.1	0.002 ± 0.001	7 ± 2
	50	1.7 ± 0.5	-16.4 ± 0.2	0.002 ± 0.001	11 ± 2	50	1.3 ± 0.3	-16.1 ± 0.1	0.0019 ± 0.0005	9 ± 2
I2	20	1.6 ± 0.4	-15.7 ± 0.2	0.006 ± 0.002	6 ± 1	20	1.7 ± 0.3	-15.5 ± 0.1	0.007 ± 0.001	7 ± 2
	30	1.9 ± 0.3	-15.6 ± 0.1	0.0030 ± 0.0005	8 ± 2	30	1.7 ± 0.3	-15.5 ± 0.1	0.004 ± 0.001	10 ± 2
	40	1.9 ± 0.3	-15.6 ± 0.1	0.0022 ± 0.0003	11 ± 2	40	1.7 ± 0.3	-15.5 ± 0.1	0.003 ± 0.001	12 ± 3
	50	1.9 ± 0.3	-15.6 ± 0.1	0.0017 ± 0.0003	13 ± 2	50	1.7 ± 0.3	-15.5 ± 0.1	0.0024 ± 0.0004	15 ± 3
I3	20	2.6 ± 0.6	-16.6 ± 0.2	0.003 ± 0.001	6 ± 1	20	2.2 ± 0.3	-16.5 ± 0.2	0.005 ± 0.001	7 ± 2
	30	2.6 ± 0.6	-16.6 ± 0.2	0.002 ± 0.001	7 ± 2	30	2.2 ± 0.3	-16.5 ± 0.2	0.003 ± 0.001	9 ± 2
	40	2.6 ± 0.6	-16.6 ± 0.2	0.0015 ± 0.0004	9 ± 2	40	2.2 ± 0.3	-16.5 ± 0.2	0.0021 ± 0.0004	11 ± 3
	50	2.6 ± 0.6	-16.6 ± 0.2	0.0012 ± 0.0003	11 ± 2	50	2.2 ± 0.3	-16.5 ± 0.2	0.0017 ± 0.0003	14 ± 3
I4	20	3.2 ± 0.8	-15.3 ± 0.3	0.003 ± 0.001	7 ± 2	20	1.4 ± 0.3	-16.4 ± 0.1	0.006 ± 0.001	5 ± 1
	30	3.2 ± 0.8	-15.3 ± 0.3	0.002 ± 0.001	9 ± 2	30	1.4 ± 0.3	-16.4 ± 0.1	0.003 ± 0.001	6 ± 2
	40	3.2 ± 0.8	-15.3 ± 0.3	0.0014 ± 0.0004	11 ± 3	40	1.4 ± 0.3	-16.4 ± 0.1	0.003 ± 0.001	8 ± 2
	50	3.2 ± 0.8	-15.3 ± 0.3	0.0011 ± 0.0003	14 ± 3	50	1.4 ± 0.3	-16.4 ± 0.1	0.002 ± 0.001	10 ± 3

^aNote that these FWHM overestimate those obtained with the ^{15}N isotopologues since N_2H^+ has a spectral resolution higher than the physical FWHM.

^bOpacity of the main hyperfine component.

Table C3. Values obtained with the fitting procedure described in Section 3.3 to the $\text{N}_2\text{H}^+(1-0)$, $^{15}\text{NNH}^+(1-0)$, and $\text{N}^{15}\text{NH}^+(1-0)$ transitions towards D1, D2, and D3. The upper limits and tentative detections are obtained as explained in Section 3.3.1.

Source	T_{ex} (K)	FWHM ^a (km s ⁻¹)	$\text{N}_2\text{H}^+(1-0)$			N_{tot} ($\times 10^{13}$ cm ⁻²)
			v_{LSR} (km s ⁻¹)	τ		
D1	20	10.0 ± 0.7	-15.0 ± 0.4	0.14 ± 0.02		4.9 ± 0.8
	30	10.0 ± 0.7	-15.0 ± 0.4	0.087 ± 0.008		6 ± 1
	40	10.1 ± 0.7	-15.0 ± 0.4	0.063 ± 0.006		8 ± 2
	50	10.1 ± 0.7	-15.0 ± 0.4	0.049 ± 0.004		10 ± 2
D2	20	8.9 ± 0.9	-14.4 ± 0.4	0.12 ± 0.02		3.7 ± 0.7
	30	9.0 ± 0.9	-14.4 ± 0.4	0.075 ± 0.009		4.9 ± 0.9
	40	9.0 ± 0.9	-14.4 ± 0.4	0.054 ± 0.007		6 ± 1
	50	9.0 ± 0.9	-14.4 ± 0.4	0.042 ± 0.005		7 ± 2
D3	20	9 ± 1	-14.8 ± 0.5	0.11 ± 0.02		3.4 ± 0.7
	30	9 ± 1	-14.7 ± 0.5	0.069 ± 0.01		4.5 ± 0.9
	40	9 ± 1	-14.7 ± 0.5	0.050 ± 0.007		6 ± 1
	50	9 ± 1	-14.7 ± 0.5	0.039 ± 0.006		7 ± 2

Source	T_{ex} (K)	FWHM (km s ⁻¹)	$^{15}\text{NNH}^+(1-0)$			$\text{N}^{15}\text{NH}^+(1-0)$				
			v_{LSR} (km s ⁻¹)	τ^b	N_{tot} ($\times 10^{11}$ cm ⁻²)	T_{ex} (K)	FWHM (km s ⁻¹)	v_{LSR} (km s ⁻¹)	τ^b	N_{tot} ($\times 10^{11}$ cm ⁻²)
D1	20				≤2	20				≤2.4
	30				≤2.6	30				≤3.2
	40				≤3.3	40				≤4
	50				≤4	50				≤4.9
D2	20	0.8 ± 0.2	-15.1 ± 0.1	0.002 ± 0.001	1.1 ± 0.4 ^c	20				≤2.4
	30	0.8 ± 0.2	-15.1 ± 0.1	0.0014 ± 0.0005	1.5 ± 0.6 ^c	30				≤3.3
	40	0.8 ± 0.2	-15.1 ± 0.1	0.0010 ± 0.0004	1.9 ± 0.7 ^c	40				≤4.2
	50	0.8 ± 0.2	-15.1 ± 0.1	0.0008 ± 0.0003	2.4 ± 0.8 ^c	50				≤5
D3	20				≤1.4	20				≤1
	30				≤1.8	30				≤1.4
	40				≤2.3	40				≤1.7
	50				≤2.8	50				≤2.1

^aNote that these FWHM overestimate those obtained with the ^{15}N isotopologues since N_2H^+ has a spectral resolution higher than the physical FWHM.

^bOpacity of the main hyperfine component.

^cTentative detection.

Table C4. Values obtained with the fitting procedure described in Section 3.3 to the $\text{N}_2\text{H}^+(1-0)$, $^{15}\text{NNH}^+(1-0)$, and $\text{N}^{15}\text{NH}^+(1-0)$ transitions towards mm1 and mm3 in regions equals to the IRAM-30m beam (see Section 3.3.2).

Source	T_{ex} (K)	FWHM ^a (km s ⁻¹)	$\text{N}_2\text{H}^+(1-0)$			N_{tot} ($\times 10^{13}$ cm ⁻²)
			v_{LSR} (km s ⁻¹)	τ		
mm1	43	10.0 ± 0.7	-14.8 ± 0.4	0.061 ± 0.006		9 ± 2
mm3	18	9.9 ± 0.6	-14.7 ± 0.3	0.18 ± 0.02		5.0 ± 0.8

Source	T_{ex} (K)	FWHM (km s ⁻¹)	$^{15}\text{NNH}^+(1-0)$			$\text{N}^{15}\text{NH}^+(1-0)$				
			v_{LSR} (km s ⁻¹)	τ^b	N_{tot} ($\times 10^{11}$ cm ⁻²)	T_{ex} (K)	FWHM (km s ⁻¹)	v_{LSR} (km s ⁻¹)	τ^b	N_{tot} ($\times 10^{11}$ cm ⁻²)
mm1	43	1.7 ± 0.3	-16.1 ± 0.1	0.0009 ± 0.0001	4.1 ± 0.7	43	2.1 ± 0.4	-16.2 ± 0.2	0.0008 ± 0.0002	5 ± 2
mm3	18	1.9 ± 0.4	-15.8 ± 0.1	0.0022 ± 0.0004	2.3 ± 0.4	18	1.8 ± 0.3	-16.1 ± 0.2	0.003 ± 0.001	2.6 ± 0.7

^aNote that these FWHM overestimate those obtained with the ^{15}N isotopologues since N_2H^+ has a spectral resolution higher than the physical FWHM.

^bOpacity of the main hyperfine component.

This paper has been typeset from a \LaTeX file prepared by the author.